Galaxy rotation favors prolate dark matter haloes

Adriana Bariego-Quintana, Felipe J. Llanes-Estrada, and Oliver Manzanilla Carretero
Universidad Complutense de Madrid, Departamento de Física Teórica and IPARCOS, Plaza de las Ciencias 1, 28040 Madrid, Spain

(Received 18 April 2022; accepted 26 March 2023; published 21 April 2023)

The flattening rotation velocity $v(r) \to$ constant found by Vera Rubin and collaborators and very apparent in the SPARC (Spitzer photometry & accurate rotation curves) galaxy–rotation data coincides with Kepler's law in one less dimension. Thus, it is naturally reproduced by elongated dark matter distributions with the axis of prolateness perpendicular to the galactic plane. This theoretical understanding is borne out by the detailed fits to the rotation data that we here report: for equal dark matter profile, elongated distributions provide smaller χ^2 than purely spherical ones. We also propose to use the geometric mean of the individual halo ellipticities, as opposed to their arithmetic average, because the ratio of the ellipsoid's minor to major half-axes $s = c/a \in (0, \infty)$ corresponds to spherical haloes for $s = 1$, so that the usually reported average is skewed toward oblateness and fails to reveal the large majority of prolate haloes. Several independently coded fitting exercises concur in yielding $s < 1$ for most of the database entries and the oblate exceptions are understood and classified. This likely prolateness is of consequence for the estimated dark matter density near Earth.

DOI: 10.1103/PhysRevD.107.083524

I. INTRODUCTION: GALACTIC ROTATION

The rotation curve $V(r)$ of a spiral galaxy is the average of the rotational speed of stars and gas versus their radial distance to the galactic center and is accessible by the Doppler effect [1–3]. Spiral galaxies equilibrate the centripetal acceleration of their distinct rotation with, presumably, their gravitational field. Therefore, from their rotation curves $V(r)$, we should be able to extract their mass distribution.

The first measured rotation curve, of M31, dates from 1939 [4]. Horace Babcock found higher values of the rotational speed than expected from observations, implying that the mass-to-light ratio $\Upsilon = M/L$ increased radially. This was initially attributed to interstellar extinction or the need to introduce new dynamic effects. Since the late 1950s rotation curves have been measured with the Doppler effect on the HI line (21 cm) [5,6]; for long, the discrepancy between the visible mass, derived from photometry, and the dynamical mass, derived from the rotation curve, was ascribed to the presence of dwarf stars and intergalactic dust and gas [7].

The work of Vera Rubin and Kent Ford in the late 1960s and early 1970s was crucial to understand rotation curves. Their improved accuracy led Vera Rubin [8] to discover the general flattening $V(r) \to$ constant of the rotation curves at large r, establishing the mass discrepancy as a general rule. Since then, rotation curves have remained a current topic of research to address the nature [9] and distribution of dark matter [10].

The renowned observational mass discrepancy arises from multiwavelength observations of galaxies, localizing visible matter within a finite volume [11], in whose interior the rotation curve should increase[1] ($V'(r) > 0$), but outside which it should decrease ($V'(r) < 0$). Outside a spherical distribution, or any distribution at sufficient distance, $g = \frac{Gm}{r^2}$ means that

$$V = \sqrt{Gm/r} \neq \text{constant} \tag{1}$$

at variance with observations; instead of declining, measured rotation curves quite generically become independent of radius $V \sim$ const (see Fig. 2 below).

Extinction by gas and dust cannot explain the mass defect: although in the visible the apparent mass would be lower, in the infrared it would increase as it is the region of gas and dust emissions. Thus, we need to adopt one of two hypotheses, either the existence of invisible dark matter, or the failure of the theoretical tools requiring modified gravitational or dynamical theories.

Among the solutions proposed to this problem, the approach of [12] is of particular interest for this work: a cylindrical source of gravitational field with mass per unit length λ yields precisely

$$V(r) = \sqrt{2G\lambda} \tag{2}$$

[1]This is usually exemplified by a solid sphere of constant density $\rho = \rho_0\Theta(r - r_0)$, with gravitational field obtained from Eq. (5), where the mass enclosed at radius r is $m = \frac{4\pi}{3}r^3$ for $r < r_0$ and $m = \frac{4\pi}{3}R^3$ for $r > r_0$. Thus, the gravitational field $g \propto r$ linearly increases inside the sphere.

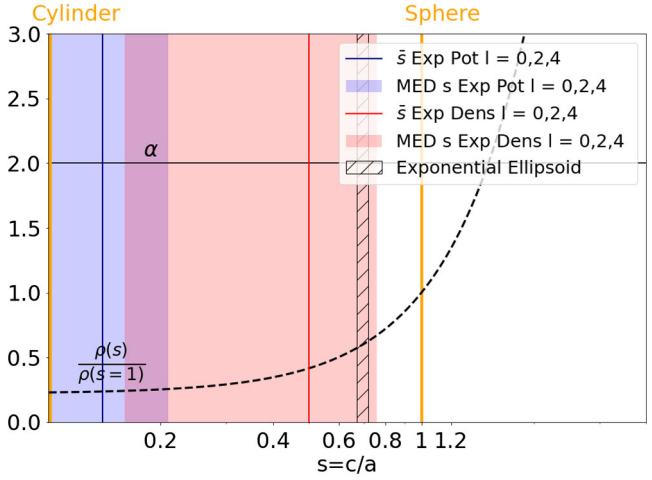

FIG. 1. Typical DM haloes fit to rotation-curve database are clearly prolate, as indicated by the median ellipticity: shown are two calculations within an angular expansion, (Secs. V B and V C) and a nonspherical ellipsoidal model (Sec. V A) that could *a priori* have been either prolate or oblate. A few outliers described below induce the uncertainty on the averages. The prolateness is in qualitative agreement with simulations (Sec. VI A) and is true for generic dark matter profiles; however, if the exponent of the dark matter profile $\alpha = -\frac{\log \rho_{\rm DM}}{d \log r}$ is near the isothermal value of 2 (horizontal line as a reminder), the shape cannot be decided, as there is a degeneracy between this fine-tuned spherical profile and the prolate shape. A curve detailing typical DM density in the galactic plane is also shown.

(from the field in Eq. (6) below). While that constancy of V extends to the largest r measured, because data covers in the end only finite r, an exactly cylindrical/filamentary contribution may not be needed, and a prolate dark matter halo may suffice. In this work we report on statistical estimates, with theory fits to the database, about the optimal prolateness that observed galactic rotation curves require. Figure 1 shows the main result of the article: the statistical distribution of rotation curves does suggest prolate haloes.

That the analysis of galactic rotation curves can be performed with Newtonian dynamics follows from typical velocities ~ 100 km/s, four orders of magnitude lower than the speed of light, and gravitational potentials of order of the Milky Way's. With $M \sim 10^{12} M_\odot$, $R \sim 30$ kpc, $\Phi \approx \frac{GM}{R} \sim 10^{11}$ m^2/s^2, and $|\frac{\Phi}{c^2}| \sim 10^{-5} \ll 1$. Hence, all conditions for the Newtonian limit are fulfilled and general relativity is unnecessary. This allows to study the gravitational field and the rotation curves within the Newtonian framework or modifications thereof, with relativity bringing about only corrections that are computable [13] but modest.

The total gravitational field is the linear superposition of those of the different source components. If there are N such components, circular orbital equilibrium reads

$$\frac{V^2}{r} = -\sum_i^N g_r|_i, \tag{3}$$

where the radial component of the gravitational acceleration field g_r follows from either the gravitational potential Φ as $g_r = -\frac{\partial \Phi}{\partial r}$ or directly from the mass density ρ through Gauss' law,

$$\int_{\partial\Omega} \vec{g} d\vec{S} = -4\pi G m. \tag{4}$$

With $m = \int_\Omega \rho dV$ interior to Ω. Choosing the boundary surface $\partial\Omega$ as equipotential, we have of course

$$g = -\frac{4\pi G m}{S}. \tag{5}$$

The modulus g and radial component g_r of the gravitational field coincide on the galactic plane under azimuthal symmetry around OZ. Thus, the expected rotation curve $V(r)$ depends on the parametrization of the gravitational potential or the mass density (these are connected through Poisson's equation $\nabla^2 \Phi = 4\pi G\rho$).

The puzzle of the constant rotation velocity has a natural solution [12] that can arise either in the dark matter or in the modified gravity scenarios, that of an elongated matter source. Indeed, in the limit of a perfect cylindrical source of linear mass density λ, the external field

$$g = \frac{2G\lambda}{r} \tag{6}$$

immediately yields $V(r) =$ constant. This can also be achieved by modifying gravity so that, in effect, there is one less dimension, such as in MOND—modified Newtonian mechanics—(or, newly, in fractional gravity [14,15]).

A. Summary of findings

There have been recent attempts at fitting galactic rotation curves with nonspherical distributions; their results seem to be contradictory. While Zatrimaylov [16] seems to concur with our observation that filamentary sources offer a better fit, Loizeau and Farrar [10] seem to find that a disk-shaped DM component could be at play, more in agreement with vintage work by Blanco and Mercader [17].

In this work we try to clarify the situation with systematic fits to as large a subset of the SPARC database as is possible to obtain a positive number of degrees of freedom in each situation, with several approaches. We first examine traditional dark matter parametrizations (with spherical geometry), MOND, and elongated geometries, against that database of spiral rotation curves, with mixed results, in which both spherical or cylindrical geometries can describe the data with a modest but sufficient parameter number to provide some flexibility. This probably explains a part of earlier discrepancies. Spherical geometries however need mass models that are similar to the isothermal one $\rho(r) \propto r^{-2}$ whereas cylindrical geometries do not need this restriction.

We then turn to a systematic multipolar expansion of the gravitational potential, and to an alternative multipolar expansion of the DM density. In both cases, with a fixed profile as function of the distance that is not the typical isothermal $\rho(r) \sim 1/r^2$ or more complicated forms that mimic this in some radial interval [18], but rather arbitrary ones such as exponentials, step functions or their softened Woods-Saxon profiles, for example, we find that the rotation data prefers an elongated source. We characterize this elongation by an ellipticity variable $s \coloneqq (c/a) = (b/a)$ that speaks of a rather prolate ellipsoidal distribution.

The distribution over the galaxy population in terms of the ellipticity is best described in logarithmic scale, since $s \in (0, 1)$ corresponds to a prolate halo (what we find), $s = 1$ to a spherical halo and $s \in (1, \infty)$ to an oblate one: the geometric mean is more reliable than the arithmetic one to avoid biasing the average to more oblate distributions.

A preliminary brief summary of our results was presented to the EPS-HEP 2021 conference [19]. This manuscript is the full documentation of the effort.

B. Dark matter radial profiles and number of parameters

Each density parametrization has a number of degrees of freedom, which is the sum of the number of free parameters and "hidden parameters," so called because they are prefixed free parameters without a clear physical motivation. These parameters are irrelevant within one fixed model, since the χ^2 is obtained by fitting the remaining parameters.

However, when comparing across models, the comparison needs to be fair: intrincate functional forms with numbers set "by eyeball" that do not follow from a theory computation are reasonably expected to better fit the data than simpler parametrizations without those numbers. If the two models would equally well describe the experimental points, which of the two would be preferable? Most people would agree that the simpler one (by Occam's razor) would be chosen. Our take on it is that each hidden parameter carries a degree of arbitrariness, since its numerical value, not derived from theory, has been selected by the inventor of the parametrization to better describe the data. Thus, it should be discounted from the number of degrees of freedom, although it may not have been systematically varied in the computer fit.

For example, Navarro-Frenck-White's parametrization (NFW) [20] in Eq. (8) is a specific case of Hernquist's [21] in Eq. (7) for $\alpha = 1$, $\beta = 1$ and $\gamma = 2$.

$$\rho_{\rm H}(r) = \frac{\rho_0}{(\frac{r}{r_0})^\alpha [1 + (\frac{r}{r_0})^\beta]^\gamma} \rightarrow \tag{7}$$

$$\rho_{\rm NFW}(r) = \frac{\rho_0}{\frac{r}{r_0}(1 + \frac{r}{r_0})^2}. \tag{8}$$

These three exponents are "hidden parameters," as they have no obvious physical motivation. The degrees of freedom for the NFW parametrization would be 5: the three prefixed exponents and the characteristic density and radius ρ_0 and r_0. Note that the 1 that is adding in the denominator is not a "hidden parameter." If we replaced the 1 by 2, it could be reabsorbed by redefining the free parameters as $r_0 \rightarrow 2r_0$ and $\rho_0 \rightarrow \rho_0/8$, yielding the starting point with the 1 instead of the 2.

This number of parameters is used for the computation of each χ^2 per degree of freedom, and will be listed for each dark matter parametrization below in Sec. II. The impact of this choice is quite small: we will find that, given the large number of experimental points, models with more parameters often yield better fits in spite of our penalizing the number of degrees of freedom, because they can more flexibly adapt to the data.

C. Use of observational data

To study the galactic rotation curves we use the SPARC database [3]. It contains, for a set of 175 galaxies, rotation curves measured from the Doppler effect in the HI and Hα lines. Furthermore, in the SPARC database the individual contributions to the rotational speed from the visible bulge $V_{\rm bulk}$, visible disk $V_{\rm disk}$ and visible gas $V_{\rm gas}$ are all estimated, based on surface photometry of galaxies at 3.6 μm. This allows to calculate the expected rotation curve due to the total visible matter $V_{\rm vis}(r)$ using

$$V_{\rm vis} = \sqrt{|V_{\rm gas}|V_{\rm gas} + \Upsilon_{\rm disk}|V_{\rm disk}|V_{\rm disk} + \Upsilon_{\rm bulk}|V_{\rm bulk}|V_{\rm bulk}}. \tag{9}$$

Therein, the criterion adopted by the SPARC collaboration [1] for the mass-to-light ratios Υ at 3.6 μm is $\Upsilon_{\rm bulk} = 1.4\Upsilon_{\rm disk}$ and $\Upsilon_{\rm disk} = 0.5 M_\odot/L_\odot$, where $M_\odot/L_\odot$ is the mass-to-light ratio for the Sun. These values come from stellar population synthesis (SPS) models, and provide the best fit for the Tully-Fisher relation [22,23]. We adopt their extracted visible matter distributions.

A typical example rotation curve, that of UGC08699, is shown in Fig. 2 together with the estimated contributions of the different matter components. Of note is a strong correlation between the variation of the distribution of visible matter and the variation of the $V(r)$ data. The large values of $V(r)$ at $r < 5$ kpc seem to be due to the dominant bulge. The two maxima in the disc contribution caused by the spiral arms produce an oscillation in the rotation curve at 5–10 kpc. The gas is just important for $r > 12$ kpc, where its contribution slightly counteracts the decrease of that of the bulge and disc. Thus, the variations of the rotation curves can be explained by the variations of the distribution of visible matter (this is Sancisi's rule [24]). Still, it is insufficient to reproduce the overall level of $V(r)$

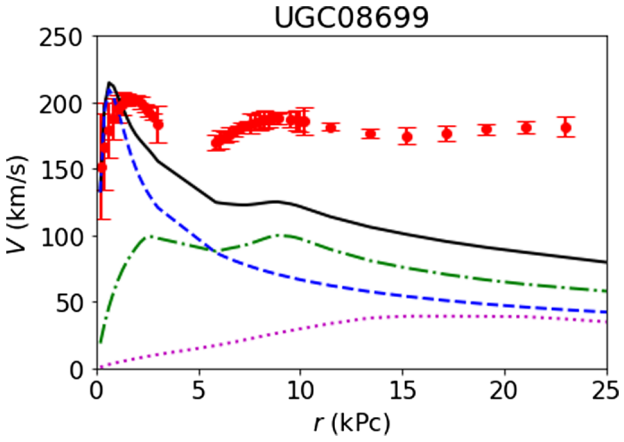

FIG. 2. Rotation curve $V(r)$ of UGC08699 (circles with uncertainty bar, red). The contributions from the bulge $V_{\rm bulk}(r)$ (dashed line, blue), the disk $V_{\rm disk}(r)$ (dashed-dotted line, green) and the gas $V_{\rm gas}(r)$ (dotted line, pink), as well as the sum of them $V_{\rm vis}(r)$ (solid black line with the highest value) to $V(r)$ are separately plotted. Observational data from the SPARC database [3]. A clear mass deficit is visible and is typical of spiral galaxies.

beyond $r \sim 2$ kpc, and dark matter or modified gravity is called for.

D. Organization of the rest of the article

In the following Sec. II we explore the hypotheses that attempt to explain the flattening of the rotation curve, adopting 9 different models (three each for MOND variants, for a spherical dark matter halo, and for non-spherical halos) for which we calculate the expected rotation curve. To compare them, we fit the maximum possible subset from the SPARC database [3], obtaining the χ^2 per degree of freedom of each fit, and aggregating all their information in a statistical analysis.

Then in Sec. III, fixing the density profile as function of the variable r to a softened step (to gain sensitivity to the halo shape that $1/r^2$ distributions do not have), we turn to a systematic multipole analysis of the gravitational potential and fit $V(r)$ once more. Here we find distorted and even cylindrical distributions to clearly provide better overall fits than purely spherical ones.

A variation of that same analysis is provided in Sec. IV, where we incorporate a multipole expansion into the DM density function $\rho(r,\theta)$ instead of the potential (that is later calculated by numerical integration). The procedure has thus different systematics from the earlier fits in Sec. III though with compatible results.

In Sec. V we turn to two independent extractions of the DM halo ellipticity from the SPARC rotation curves. As stated, we find that the quantity $\langle \log(s) \rangle$ provides a more convincing assessment, in a statistical sense, than simply $\langle s \rangle$.

Section VI wraps the discussion up, in particular comparing our observational data extraction to numerical simulations; and an Appendix A 1 collects and classifies the few galaxies among the fitted SPARC ones that contradict our statement that prolateness is the preferred explanation of rotation curves, by yielding instead an oblate fit, and in a separate table, those that seem to have observational issues or too much structure (intense oscillations) likely not related to dark matter.

II. CLASSIFICATION OF VARIOUS MODELS BY χ^2

In this section we then proceed to contrast traditional approaches to Dark Matter at galactic scales and deformed haloes against the database. Let us first describe each of the models individually.

A. Modified Newtonian dynamics

MOND [25–27] hypothesises the failure of Newtonian dynamics at low accelerations, of the order of a new universal constant a_0. In this regime, MONDian acceleration would be $a = \sqrt{a_N a_0}$, where a_N is the Newtonian one. The flattening of rotation curves then becomes a consequence of this transition, designed *ad-hoc* to avoid the need for a dark matter halo. Supposing a compact spherical visible mass distribution of mass, the outside gravitational field would change from $a_N = g \propto r^{-2}$ to $a = V^2/r = \sqrt{a_N a_0} \propto r^{-1}$, and lowering that power makes $V(r)$ constant.

To soften the nonanalyticity caused by that prescription, interpolating functions are used,

$$\mathbf{F} = m\mathbf{a}\,\mu\left(\frac{a}{a_0}\right), \tag{10}$$

where $\mu(x)$ is an appropriate function behaving as $\mu(x) \approx x$ at low-x yielding $a = \sqrt{a_N a_0}$, but as $\mu(x) \approx 1$ at high-x, eliminating the correction $a = a_N$. Often used such functions are the so-called "standard" and "simple" proposed by Milgrom [26] and Famaey and Binney [28], respectively. These are given by $\mu_{\rm Standard}(x) = \frac{x}{\sqrt{1+x^2}}$ and $\mu_{\rm Simple}(x) = \frac{x}{1+x}$ yielding

$$a_{\rm Standard} = \frac{1}{2}\left(a_N^2 \pm \sqrt{a_N^4 + 4a_N^2 a_0^2}\right)^{\frac{1}{2}} \tag{11}$$

$$a_{\rm Simple} = \frac{1}{2}\left(a_N \pm \sqrt{a_N^2 + 4a_N a_0}\right). \tag{12}$$

As Fig. 3 shows, the transition between the Newtonian and MOND (low x) regimes is sharper in the "standard" case, spreading to larger x values in the "simple" one.

The difference between the MONDian and Newtonian frameworks are noticeable in Fig. 4, where we fit to UGC08699 data. Visible matter, from Eq. (9), with

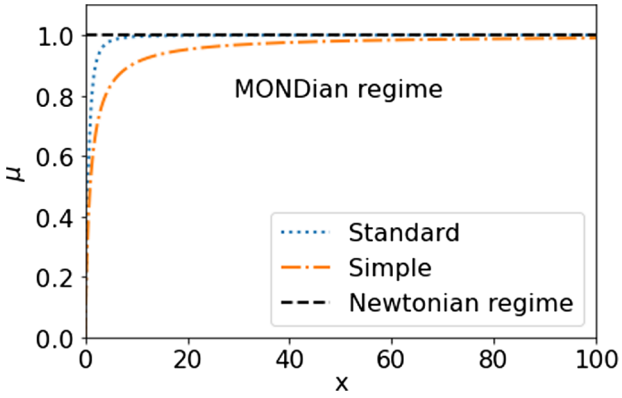

FIG. 3. Function $\mu(x)$ for "simple" and "standard" expressions in Eqs. (11) and (12).

Kepler's law, yields the dotted curve that is in gross disagreement for $r > 3$ kpc. Employing instead MOND Standard, Eq. (11), and Simple, Eq. (12), yields acceptable fits, best for $a_0 = (2.24 \pm 0.05) \times 10^{-10}$ m/s^2 with $\chi^2/N_F = 1.8$ for MOND Standard, and $a_0 = (1.63 \pm 0.04) \times 10^{-10}$ m/s^2 with $\chi^2/N_F = 0.97$ for MOND Simple.

MOND in the relevant parameter range can only with difficulty be challenged by solar-system physics. Earth's gravitational field would have decreased to the magnitude of a_0 at a distance $d \sim 13.4$ a.u., so the severe consequences of the transition from Newtonian to MONDian acceleration could be seen around Pluto's orbit, $d \sim 39.48$ au; but there, Earth's influence respect to the Sun and other bodies is negligible, e.g., $(a_\oplus^{\rm MOND} - a_\oplus)/a_\odot \sim 10^{-5}$, five orders of magnitude smaller than the Sun's gravitational field. For the Sun, the MOND's acceleration correction only reaches 10% ($a_\odot^{\rm MOND} = 1.1 a_\odot$), at $d \approx 2000$ au, close to the hypothetical Oort cloud.

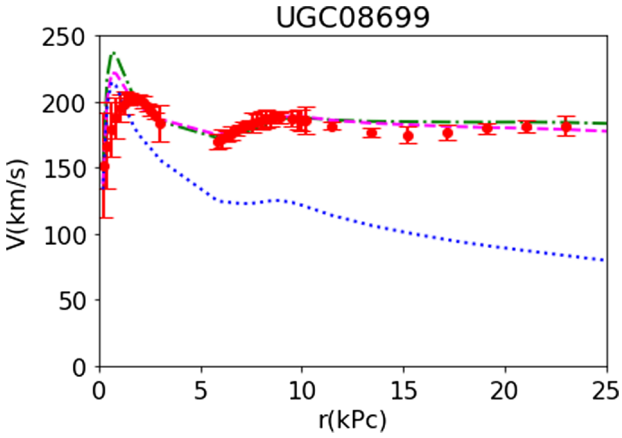

FIG. 4. We fit the rotation curve (circles with uncertainty bars) of UGC08699 [3] using MOND standard (dashed-dotted, green) and simple (dashed, pink) from the estimated rotation curve due to visible matter (dotted, blue, corresponding to Newtonian mechanics).

The main problem that MOND faces is that the phenomenology of the cosmos at larger than galactic scales is marginally reproduced at best: it has difficulties in reproducing cosmic microwave background anisotropies [29], the velocity dispersion and temperature profiles from galaxy clusters [30], and some events such as the Bullet Cluster [31] without introducing dark matter, thus losing its main attraction. This same observation applies to multiple attempts at modifying gravity, e.g., via the Lanczos tensor [32].

B. Dark matter haloes

The rest of the models that we will fit are consistent with the most widely held hypothesis that the flattening of $V(r)$ is due to a dark matter (DM) halo, invisible at basically any wavelength. Depending on the type of DM and its self-interactions, the formation of structure can be faster or slower. Some simulations with light DM particles, such as "fuzzy" DM, produce halos that are filamentary and diffuse, and as the DM-particle mass increases, the halo shapes become lumpy [33,34]. Hence, knowing the typical shape of halos from galaxy data can be important to address the mass (or equivalently, the Avogadro number and speed) of DM particles.

From the SPARC velocity curves and their estimates for the visible matter component, we can derive a dark contribution to the rotation curve $V_{\rm DM}$ that we in the following use as pseudodata,

$$V_{\rm Tot}^2 = V_{\rm DM}^2 + V_{\rm vis}^2, \tag{13}$$

whereas when $V_{\rm vis}^2 > V_{\rm Tot}^2$ we will set $V_{\rm DM} = 0$.

1. Spherical dark matter haloes ($r \equiv \sqrt{x^2+y^2+z^2}$)

These have been usually assumed by analogy with other astrophysical bodies, and have the gravitational field of Eq. (5), with a mass internal to the spherical surface at r of $m = 4\pi \int_0^r r'^2 dr' \rho(r')$, yielding

$$g(r) = \frac{4\pi G}{r^2} \int_0^r r'^2 dr' \rho(r'). \tag{14}$$

The rotation curve $V(r)$ is then

$$V(r) = \sqrt{4\pi G \int_0^r r'^2 dr' \frac{\rho(r')}{r}}. \tag{15}$$

To proceed, the radial profile $\rho(r)$ needs to be specified. We will employ some of the most widely used ones in the literature.

Navarro-Frenk-White parametrization.—Navarro *et al.* [20] carried out N-body simulations and found that their simulated halos follow an approximate density profile given by

$$\rho(r) = \frac{\rho_0}{\frac{r}{r_0}(1+\frac{r}{r_0})^2}. \tag{16}$$

This parametrization has five degrees of freedom: two free parameters ρ_0 and r_0, and three "hidden parameters," which are the power laws of the denominator. Because $\rho(r)$ diverges at $r \to 0$, exhibiting a "cusp" nucleus, it contradicts observational data, which shows an almost constant nucleus or "core." This discrepancy is the so-called core-cusp problem [35]. Several mechanisms such as supernovae feedback or baryonic clumps and dynamical friction have been proposed to solve the problem [36], though the topic is still open.

Additionally, because $\rho(r)$ decreases slowly, as r^{-3} at large radii, the total mass

$$M = 4\pi \int_0^\infty r'^2 dr' \frac{\rho_0}{\frac{r'}{r_0}(1+\frac{r'}{r_0})^2} = 4\pi\rho_0 r_0^3 \left[\frac{1}{1+\frac{r'}{r_0}} + \log\left(1+\frac{r'}{r_0}\right)\right]_{r'=0}^{r'\to\infty} \to \infty \tag{17}$$

has a log divergence for $r \to \infty$. This is usually solved by introducing a cutoff in the density profile $\rho(r) \to \rho(r)\Theta(R_{\rm cut} - r)$ with a step function or a softening thereof, imposed outside the visible disk to avoid distorting the rotation curve while ensuring a finite total mass M. At distances where $R_{\rm cut}$ could be noticeable, the interaction with other galaxies becomes important and asking about the mass of the individual halo stops being meaningful.[2] The same divergence appears in other parametrization such as the pseudoisothermal one (in Sec. II B 1 b below), for example.

The rotational speed of this NFW profile can be straightforwardly calculated using Eq. (15),

$$V(r) = \sqrt{\frac{4\pi G\rho_0 r_0^3}{r}\left[\log\left(1+\frac{r}{r_0}\right) - \frac{\frac{r}{r_0}}{1+\frac{r}{r_0}}\right]} \tag{18}$$

and is shown, for the case of M31, in Fig. 5.

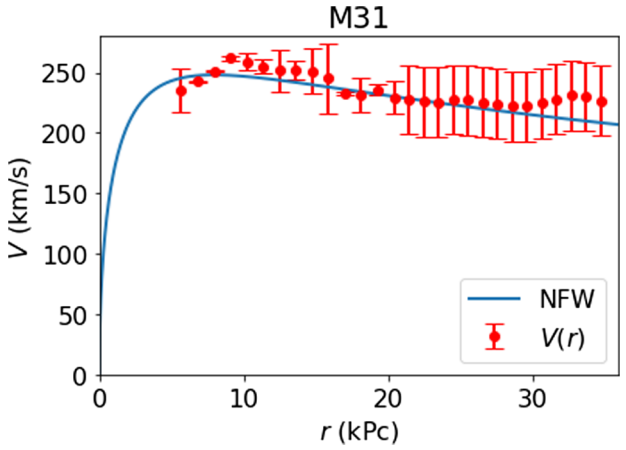

FIG. 5. We fit the rotation curve of M31 using the $V(r)$ from the NFW parametrization of Eq. (18). Observational data from Carignan *et al.* [38].

Pseudo-isothermal parametrization.—This approach requires DM self-interactions to be sufficiently strong for the halo to thermalise, reaching a homogeneous equilibrium temperature. This can happen for heavy enough DM only through gravitational interaction, and may require additional, weak interactions for WIMPs.[3] This results in an isothermal sphere [43], whose density profile is

$$\rho = \frac{\rho_0}{(r/r_0)^2}. \tag{19}$$

Its rotation curve $V(r)$ is then constant for any radius V(r) = const, as can be seen in Eq. (15) for Eq. (19). However, because the observed rotation curves are not flat but increase at small r, the denominator in Eq. (19) is empirically modified, without altering the wanted behavior at large radii. Thus,

$$\rho(r) = \frac{\rho_0}{[1+(\frac{r}{r_0})^\alpha]^{2/\alpha}}. \tag{20}$$

The most commonly used form of this profile incorporates $\alpha = 2$, which is the so-called Pseudo-isothermal parametrization [44]

$$\rho(r) = \frac{\rho_0}{1+(\frac{r}{r_0})^2}. \tag{21}$$

[2]To illustrate the point, consider the halo of M31. We can guess the M31 DM fraction from cosmological values $\Omega_M = \Omega_{\rm DM} + \Omega_b \approx 0.31$ and $\Omega_{\rm DM} \approx 0.26$ [37] to be around $\Omega_{\rm DM}/\Omega_M \sim 0.8$. Thus, from $M_{\rm M31} = 1.5 \times 10^{12} M_\odot$ and with $M_{\rm DM} \sim 0.8 M_{\rm M31}$, we can estimate $R_{\rm cut}$ from cutting off Eq. (17). The distribution parameters are fit to the M31 rotation curve $V(r)$ using Eq. (18), becoming $\rho_0 = (2.6 \pm 0.2) \times 10^{-20}$ kg/m^3, $r_0 = 3.7 \pm 0.1$ kpc with $\chi^2/N_{\rm F} = 5.2$ (see Fig. 5). Thus, the estimated cutoff radius is $R_{\rm cut} \approx 373 r_0 = 1373$ kpc; as this is larger than the distance between the Milky Way and M31 standing at $\approx$765 kpc, the cutoff is beyond the validity of the concept of an isolated spiral galaxy halo.

[3]The lack of direct DM detection sets strong bounds to possible interactions [39]. WIMP cross sections on the nucleon are by now lower than 10^{-43} cm^2, making it a poor relaxation mechanism. If we limit ourselves to a purely gravitational interaction, structure formation delimits the mass somewhere between 1 keV and 100 GeV, where the DM halos become cuspy [40]. In the case of strongly interacting massive particles (SIMP), the Earth and Uranus heat flows [41,42] exclude masses from 150 MeV to 10^4 GeV, and set an upper limit on the cross section for the self-annihilation for masses from $1 - 10^{10}$ GeV. However, the constraints still allow a wide range of masses and interactions providing thermal equilibrium.

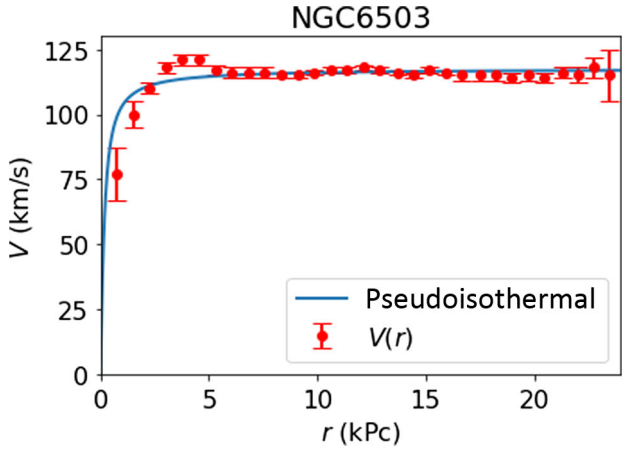

FIG. 6. We fit the rotation curve of NGC6503 using $V(r)$ with the pseudoisothermal parametrization of Eq. (22). Data from SPARC [3].

Upon integrating Eq. (15) with the density of Eq. (21), the rotational speed obtained is

$$V(r) = \sqrt{4\pi G\rho_0 r_0^2\left[1 - \frac{r_0}{r}\arctan\left(\frac{r}{r_0}\right)\right]}. \quad (22)$$

This mass distribution does not suffer from the core-cusp problem, though it then disagrees with typical N-body simulations. $\rho(r)$ is almost constant at low radii, showing a core nucleus, and the second term from $V(r)$ vanishes for large r, $V(r)$ becoming constant. Hence, an isothermal distribution at large radii explains the flattened rotation curves. This can be seen in Fig. 6, where the rotation curve of NGC6503 has been fitted with Eq. (22).

This parametrization has three degrees of freedom: the two free parameters ρ_0 and r_0, and the hidden parameter $\alpha = 2$.

Einasto profile.—Einasto *et al.* [45] proposed a density profile inspired by Sersic's law [46], consisting of an exponential of a power law. It is usually written as

$$\rho(r) = \rho_0 e^{-\frac{2}{N}\left[\left(\frac{r}{r_0}\right)^N - 1\right]}. \quad (23)$$

The physical meaning of the parameter N can be understood from Fig. 7, where we plot the Einasto profile normalized to one at its maximum, versus $x = r/r_0$: N controls the slope of the mass distribution. For values $N < 1$, the mass lies almost entirely within the characteristic radius r_0. This is the typical mass distribution for visible matter. In fact, for $N = 1/4$ we recover the de Vaucouleurs' law [47] which describes the surface brightness of elliptical galaxies and bulges. For $N > 1$, the mass fraction outside of r_0 increases. This mass fraction would play the role of DM and, therefore, the larger N adopted, the larger contribution to the gravitational field the DM provides.

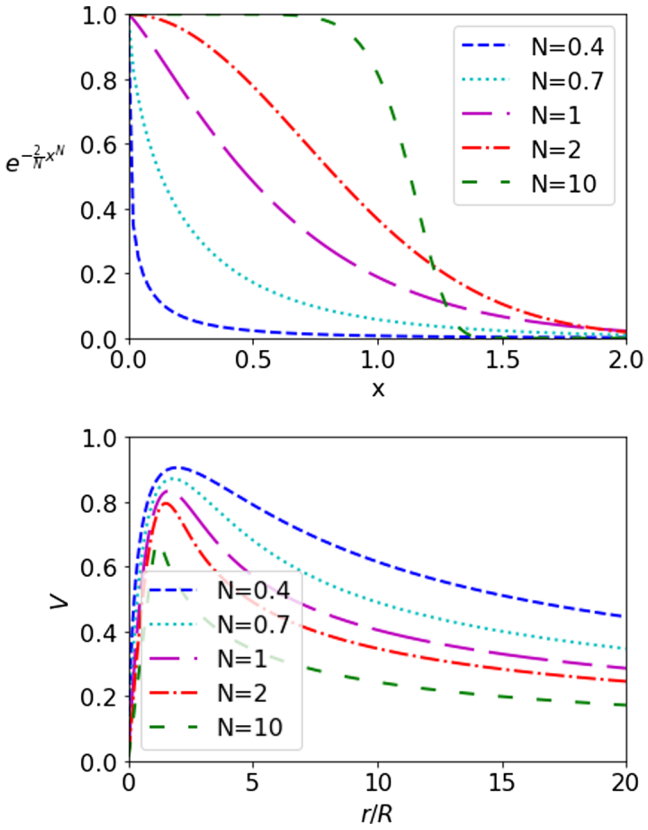

FIG. 7. Top: Einasto profiles, normalized to 1 at their maximum, for different values of the parameter N of Eq. (23). Bottom: corresponding rotation curves, with velocity normalized using $4\pi G\rho_0 r_0^2 = 1$.

The degrees of freedom of this density profile are three: the dimensional parameters ρ_0 and r_0, and the power-law index N.

We know no analytical expression for the rotational speed and calculate it numerically. Typical rotation curves for some values of N can be seen in the bottom plot of Fig. 7. They all increase until they reach a peak, from which they decay. For larger N, this falling becomes more abrupt, but outside it, the slope of the curve is lower. Note that there is no exact flattening for any value of N.

2. *Cylindrical dark matter haloes* ($r \equiv \sqrt{x^2+y^2}$)

It is not far-fetched to consider asymmetric haloes, particularly in view that visible matter is actually not symmetrically distributed, but in spiral galaxies concentrated on a disk instead. It is therefore useful to explore nonspherical halos if this would provide advantage in explaining the data.

Further, galaxy surveys, such as 6dF [48] and SDSS [49], find a large-scale anisotropic structure or "cosmic web," with walls, filaments, and voids. This structure has been

reproduced in cosmological simulations [34,50], where galaxies are connected by DM filaments that become clumpier as the mass of the DM particle or the intensity of their interaction increases. This suggests that the DM halo may have a filamentary contribution [12]. Therefore, their DM halo may be a mixture of a cylindrical contribution inherited from the filament, and a spherical contribution from the DM clump seeding the galaxy formation.

We then explore the hypothesis that DM is distributed in elongated structures down to galactic scales: in this section, we consider three models with an exactly cylindrical halo, while later we will produce interpolating parametrizations between spherical and cylindrical geometries. Instead of the spherical radial variable $r = \sqrt{x^2 + y^2 + z^2}$, for these models we adopt cylindrical coordinates and the radial distance is, instead, $r = \sqrt{x^2 + y^2} = r_\perp$. Both take the same value on the observable galactic plane where velocities are measured, of course, chosen as $z = 0$.

The gravitational field of a cylindrical source of infinite length is easily derived through Gauss's law, Eq. (4), by choosing a cylindrical surface of equation $x^2 + y^2 = r^2$ and $S = 2\pi rL$, on which the gravitational field $g(r)$ is constant, as the contour for the integral,

$$g(r) = -\frac{4\pi G m(r)}{2\pi r L}. \tag{24}$$

Therefore, the rotation curve $V(r)$ becomes

$$V(r) = \sqrt{4\pi G \int_0^r r' dr' \rho(r')}. \tag{25}$$

We are simplifying the discussion to the kinematic situation in which the major axis of the dark matter distribution is aligned with the axis orthogonal to the galactic disk, so that the entire matter and dark-matter distribution has cylindrical symmetry. If the galactic plane was instead not perfectly perpendicular to that dark-matter axis, precession around it would occur. Such motion is described, in the case of a very eccentric dark-matter ellipsoid ($s = c/a \ll 1$) in [12], and can be broken into a vertical motion parallel to the dark-matter axis which is near harmonic oscillation, and galactic in-plane motion as described in this section. The two frequencies need not match, so orbits are open.

Finite-width cylinder parametrization.—If the DM is distributed in a finite-width cylinder of constant density like Eq. (26), the rotation curve is still constant outside the DM halo, but inside it, the rotation curve increases linearly as in Eq. (27); since the mass depends on the radius as $\frac{M}{\pi R^2 L} = \frac{m(r)}{\pi r^2 L}$ we have $m(r) = M\frac{r^2}{R^2}$.

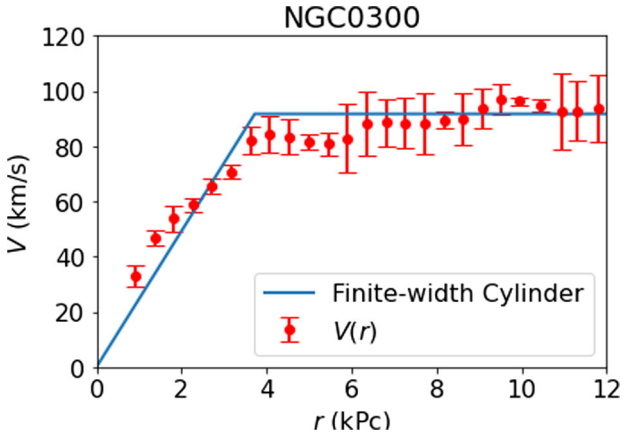

FIG. 8. We fit the rotation curve of NGC0300 using the $V(r)$ of a DM finite-width cylinder of constant density, Eq. (27). SPARC data from [3].

$$\rho(r) = \begin{cases} \frac{M}{\pi R^2 L} & \text{If r < R} \\ 0 & \text{If r > R} \end{cases} \tag{26}$$

$$V(r) = \begin{cases} \sqrt{2G\lambda}\frac{r}{R} & \text{If r < R} \\ \sqrt{2G\lambda} & \text{If r > R.} \end{cases} \tag{27}$$

The resulting $V(r)$ perfectly captures the essence of typical measured rotation curves, as shown in Fig. 8.

There are two degrees of freedom for the model fit: the linear linear density λ and the cylinder radius R.

Woods-Saxon cylinder parametrization.—A drawback of the finite-width cylinder parametrization is the density discontinuity at $r = R$, Eq. (26), and it is interesting to introduce a "skin" function that provides a smoother transition. A good choice for the "skin" function is the one in the Wood-Saxon potential, used to describe soft nuclear edges in nuclear physics [51],

$$\rho(r) = \frac{\rho_c}{1 + e^{\frac{r-R}{a}}}. \tag{28}$$

This parametrization has three degrees of freedom: the characteristics mass density and radius of the cylinder ρ_c and R, and the "skin" parameter a.

The value of a rules the smoothness of the transition at $r = R$. For $a \to 0$ the cylinder has no skin and we recover the density profile of the finite-width cylinder, while for $a \to \infty$ the skin of the cylinder is infinite and ρ becomes r-independent.

For this mass distribution the rotation curve $V(r)$ in Eq. (25) has an analytical expression as a function of polylogarithms; however, it is cumbersome and we rather calculate it numerically. As with the finite-width cylinder parametrization, the rotation curve $V(r)$ for finite a becomes asymptotically constant as $r \to \infty$. This can be seen in Fig. 9, where we fit the rotation curve of NGC0300.

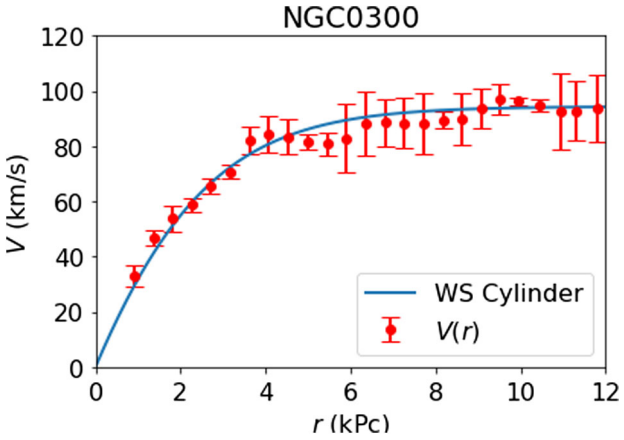

FIG. 9. We fit the rotation curve of NGC0300 using $V(r)$ for the Woods-Saxon cylinder parametrization, Eq. (28). SPARC data from [3].

The fit is much better than that of the finite-width cylinder, improving its $\chi^2/N_{\rm F} = 3.68$ to $\chi^2/N_{\rm F} = 0.852$ for the Woods-Saxon cylinder.

Generalized logarithmic potential.—The gravitational potential outside a dense filament is a simple logarithm. A version thereof with more parameter freedom to improve data fitting is treated in this subsection: we call this version Generalized logarithmic potential because it is a generalization of James Binney's [52], who used it to describe the gravitational field of flattened bodies (ironically, it is a natural potential for elongated ones),

$$\Phi(r) = \Phi_0 \log\left[C + \left(\frac{r}{R}\right)^{2\alpha}\right] \tag{29}$$

except that we allow a variable α instead of fixing it to 1.

This Generalized log potential is fully determined by the characteristic radius R, the constant Φ_0, the power law α, and the parameter C. The latter establishes the value $\Phi(0)$, and can be understood as a gauge freedom without physical impact. In fact, we can rewrite the potential as $\Phi(r) = \Phi_0 \log\left[1 + \frac{1}{C}\left(\frac{r}{R}\right)^{2\alpha}\right] + \Phi_0 \log C$, and redefine the characteristic radius $R'^{2\alpha} = R^{2\alpha}/C$ yielding

$$\Phi(r) = \Phi_0 \log\left[1 + \left(\frac{r}{R'}\right)^{2\alpha}\right] + \Phi_0 \log C. \tag{30}$$

Since the gravitational field and the mass density are derived through $\vec{g} = -\vec{\nabla}\Phi$ and $\nabla^2\Phi = 4\pi G\rho$, after defining the new characteristic radius R', both the gravitational field and mass density are independent of C. Thus, we can take $C = 1$ without loss of generality (Note that if $C = 0$ the predicted rotation curve is $V(r) = \sqrt{2\alpha\Phi_0}$ for any radius r, since $\log(r)$ is the potential due to the straight filament of Eq. (27); the finite value of C makes the potential flexible enough to describe the growth of V at low r). Thus, this potential is characterized by only three free parameters: R, Φ_0 and the power law α.

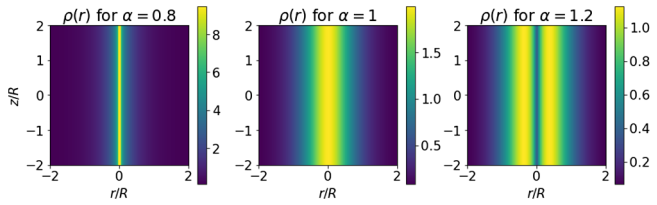

FIG. 10. Density plots of $\rho(r)$ in Eq. (31) for $\Phi_0 = 2\pi GR^2$ and different values of α, showing a cusp (left), a core (middle), and a shell-like (right) cylindrical haloes.

Poisson's equation provides the mass density profile

$$\rho(r) = \frac{\alpha^2\Phi_0}{\pi G}\frac{1}{r^2}\frac{r^{2\alpha}/R^{2\alpha}}{(1 + r^{2\alpha}/R^{2\alpha})^2} \tag{31}$$

that imposes some parameter restrictions due to the $\rho > 0$ positiveness condition, namely $\alpha > 0$ and $\Phi_0 > 0$.

Figure 10 shows $\rho(r)$ for $\Phi_0 = 2\pi GR^2$ and different values of α. For $0 < \alpha < 1$ we find cusp halos (the plot has the appearance of a narrow slit), for $\alpha = 1$ they became softer and a core appears, while for $\alpha > 1$ the core disappears and the halo is shell-like. Curiously, this later case has been observed in large-scale structure formation simulations for warm, for hot and for fuzzy DM [33,34].

In fact, we can intuitively relate α to unknown microscopic properties such as the mass of the DM particles or the intensity of their interaction. An initial velocity dispersion of the DM particles could be smaller than at equilibrium, $\sigma_V/\sigma_V^{\rm eq} \ll 1$. Their interactions would widen that dispersion: Less energetic particles populate small r orbits, while more energetic ones will be found at large radii. Therefore, $\rho(r)$ in principle conveys information about the strength of the interaction, i.e., the DM particle mass for the gravitational interaction, or its charge associated to other interactions. Heavy (or strongly interacting) DM particles concentrate at the galactic centre and generate cusp halos, while light (or weakly interacting) DM particles spread to larger radii, producing, in an extreme case, shell-like halos. This means that $0 < \alpha < 1$ corresponds to heavy (or strongly interacting) DM particles, $\alpha > 1$ to light (or weakly interacting) DM particles, and $\alpha \simeq 1$ provides the transition between the two regimes.

The predicted rotation curve is given by

$$V(r) = \sqrt{2\alpha\Phi_0\frac{r^{2\alpha}/R^{2\alpha}}{1 + r^{2\alpha}/R^{2\alpha}}}. \tag{32}$$

Note that at large radii $r/R \gg 1$, $V(r) \to \sqrt{2\alpha\Phi_0}$ becomes constant for fixed α. Normalized rotation curves for some values of α can be seen in Fig. 11.

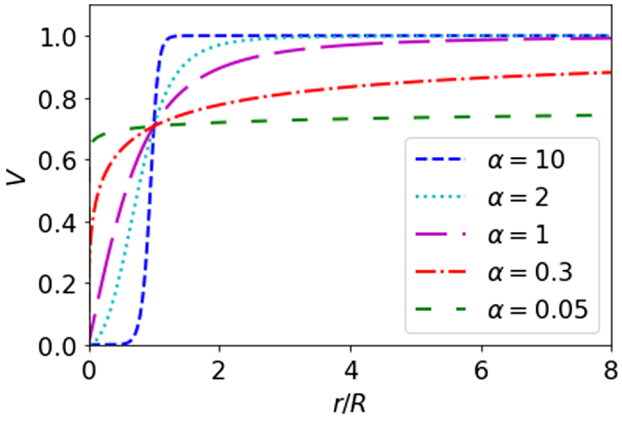

FIG. 11. Shape of the rotation curves of the generalized logarithmic potential for different values of α, where the velocity has been normalized to $V(R) = 1/\sqrt{2}$.

C. Data and analysis

We now proceed to compare the nine model approaches described so far, ordering them on the basis of their ability to reproduce the observed rotation curves. For this purpose, we perform a least-squares fit of each rotation curve of the SPARC database [3], minimizing χ^2 as a function of the free parameters of the model,

$$\chi^2 = \sum_{i=1}^{N} \frac{[V_i^{\rm obs} - V^{\rm th}(r_i)]^2}{\Delta V_i^{\rm obs\,2}}. \tag{33}$$

Therein, $V_i^{\rm obs} \pm \Delta V_i^{\rm obs}$ is the experimental rotation curve with its uncertainty, and $V^{\rm th}$ the model prediction.

For the six models that involve dark matter (three with spherical and three with cylindrical geometry) we employ for $V_{\rm obs}$ the pseudo data $V_{\rm DM}$ derived in Eq. (13), so that only the dark matter contribution to the squared velocity is fit. For the three models without DM (pure Newtonian mechanics with the visible matter and MOND) we employ the measured velocity $V_{\rm obs} = V_{\rm Tot}$, without subtracting any visible contribution (as is obviously necessary in the earlier ones with DM). Also, for these models without DM we compute $V_{\rm th}$ from the estimated visible $V_{\rm vis}$: $V_{\rm vis}^2/r$ plays the role of the Newtonian acceleration $a_{\rm N}$ in Eqs. (11) and (12).

However, since each model approach has a different number of parameters, we calculate the number of degrees of freedom (d.o.f.) for each of the galaxies, calculate $\chi^2/N_{\rm F}$, with

$$N_{\rm F} = N_{\rm points} - d.o.f. \tag{34}$$

being the difference between the number of points on a given SPARC rotation curve and the number of free plus hidden parameters of the tested model.

Because $\chi^2/N_{\rm F}$ needs to be positive, we need $N_{\rm F} > 0$. Because we want to test all the models against the same sample of galaxies for a fair comparison, we only use those galaxies whose observational rotation curves exceed 5 points, which is the largest number of parameters of any of the examined models (saturated by the NFW parametrization). This reduces the sample of 175 rotation curves to 164. Besides, we are forced to exclude the rotation curve of UGC01281, since the estimated $V_{\rm vis}$ becomes complex at small radii, reflecting some observational analysis issue, leaving a total of 164 rotation curves.

For each rotation curve $V(r)$ of this subset and each of the models, we compute the optimal $\chi^2/N_{\rm F}$ over the model parameter space. The minimization is carried out employing the well established CERN's MINUIT algorithm as implemented by standard Python libraries [53], and a pass over the entire galaxy database runs in a few hours in a standard departmental Linux cluster.

Each galaxy then yields a $\chi^2/N_{\rm F}$ ranking of the nine model approaches from 1, at the smallest $\chi^2/N_{\rm F}$, to the 9th having the largest such (as summarized in Table I): the lower the model ranking number, the better the overall fit. In the case where a galaxy assigns two or more models essentially the same $\chi^2/N_{\rm F}$ (which is calculated to four digits to minimize this possibility), the rank assigned to all those with a degenerate value is the group's average, e.g., if

TABLE I. Summary of the model approaches examined against the galaxy database: mass distribution, rotation curve $V(r)$, number of degrees of freedom, number of free parameters, and whether the expected rotation curve $V(r)$ flattens out at large r.

Model	Mass distribution	$V(r)$	d.o.f.	$N_{\rm F.P.}$	Flat $V(r)$
Newtonian	Visible only	$V_{\rm vis}$	0	0	No
MOND Standard	Visible only	$V_{\rm vis}^2/r$ in Eq. (11)	2	1	Yes
MOND Simple	Visible only	$V_{\rm vis}^2/r$ in Eq. (12)	2	1	Yes
NFW	DM Eq. (16)	Eq. (18)	5	2	No
Pseudoisothermal	DM Eq. (21)	Eq. (22)	3	2	Yes
Einasto	DM Eq. (23)	Numerically	3	3	No
Finite-width cylinder	DM Eq. (26)	Eq. (27)	2	2	Yes
Woods-Saxon cylinder	DM Eq. (28)	Numerically	3	3	Yes
Generalized logarithmic potential	DM Eq. (31)	Eq. (32)	3	3	Yes

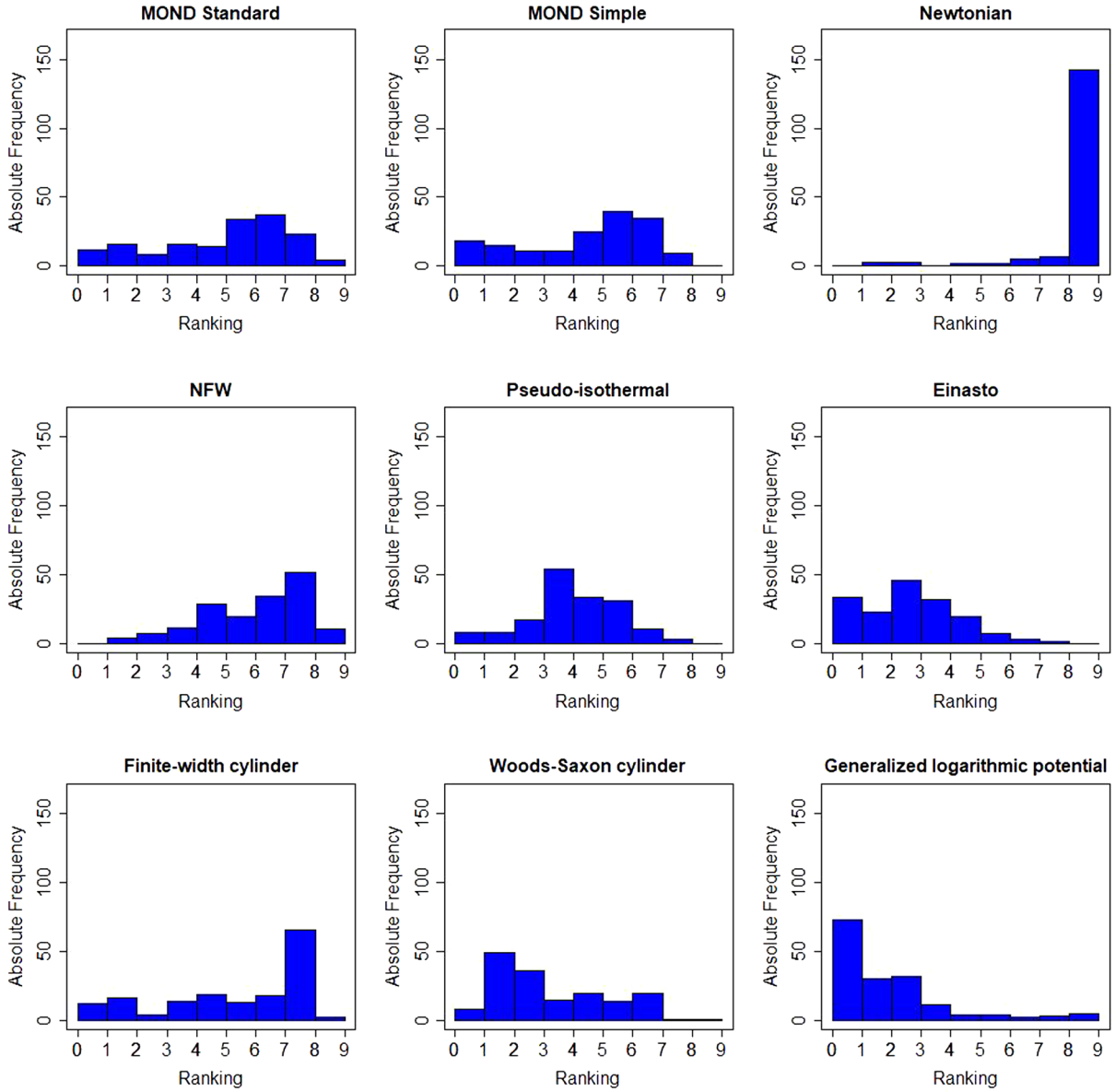

FIG. 12. Histograms of the distribution of model rankings for $\chi^2/N_{\rm F}$ for each parametrization.

two of them coincide on the smallest value of $\chi^2/N_{\rm F}$, they both receive the rank $(1+2)/2 = 1.5$.

We show histograms of these rankings in Fig. 12, where the height of the bars represents the number of galaxies that assign the given ranking (along the OX axis) to the model in the given plot. Further, in Table II we provide the parameters of the ranking distributions over the galaxy population, namely their means $\bar{x}$, medians Med, standard deviations σ, and median absolute deviations MAD.

The diversity in the measured rotation curves, not all of which extend far enough to flatten out as seems to be the norm, makes different model approaches better suited for different galaxy subsets. Such dispersion can be exposed by overall "agreement" vs "disagreement" tests (useful in other contexts to understand the opinion of jurors or committee members choosing among several options). For example, ascertaining such agreement among different galaxies we have performed Kendall's W test [54]. This is based on the matrix $r_{i,j}$ containing the rank assigned to model i by each rotation curve j. The statistical criterion is based on the number

$$W = \frac{12S}{(n^3 - n)}, \tag{35}$$

where $n = 9$ is the number of models to be compared. The numerator S is constructed from the average rank assigned to each model by each of the $m = 164$ usable rotation curves with sufficient measured data points, $R_i = \frac{1}{m}\sum_{j=1}^{m} r_{i,j}$. This is then averaged over all the models

TABLE II. Measures of centrality and dispersion of the model ranking: we give the average with standard deviation and the median with median absolute deviation of the position in which the galaxy fits prefer each of the models. Clearly, purely Newtonian physics with visible matter only yields the worse overall fits. The (purely spherical) Einasto and (purely cylindrical) logarithmic dark matter potentials yield the best fits, of comparable quality to each other, with other spherical and cylindrical approaches, having less parameters, following in the given order.

Ranking order	Model	$\bar{x} \pm \sigma$	Med $\pm$ MAD
1	Generalized log potential (cylindrical)	2.4 ± 1.9	2 ± 1
2	Spherical Einasto	3.1 ± 1.6	3 ± 1
3	Woods-Saxon cylinder	3.7 ± 1.9	3 ± 1
4	Pseudoisothermal	4.5 ± 1.5	4 ± 1
5	MOND Simple	4.9 ± 2.1	6 ± 1
6	MOND Standard	5.4 ± 2.2	6 ± 1
7/8	Finite-width cylinder	5.8 ± 2.4	7 ± 1
7/8	Spherical NFW	6.5 ± 1.7	7 ± 1
9	Newtonian	8.6 ± 1.4	9 ± 0

$\bar{R} = \frac{1}{n}\sum_{i=1}^{n} R_i$ and a quadratic deviation constructed therewith as $S = \sum_{i=1}^{n} (R_i - \bar{R})^2$.

Kendall's W values range between 0 (for largest disagreement among galaxies) to 1 (for full agreement: all would favor the same model). We obtain $W = 0.013$, and after correcting for tied rank, $W = 0.014$; because it is quite small, a large "dispersion" in the rankings, visible in Table II, is suggested. This amply justifies the further work in this article.

In spite of this dispersion, we have some statistical confidence that we may broadly order the models as in Table II from a computation of the U test of Wilcoxon-Mann-Whitney [55].

This is a nonparametric test that compares the medians according to the following criterion: given two samples of n_1 and n_2 elements, we order the total set giving each element the rank $r_{j,i}$ (the rank in the total set of the element i from the sample j), from which we calculate the parameter

$$U_2 = \sum_{i=1}^{n_2} r_{i,2} - \frac{n_2(n_2+1)}{2}. \tag{36}$$

We reject the null hypothesis that the median of sample 2 is smaller than the median of the sample 1, symbolically H_0: $\mathrm{Med}_2 < \mathrm{Med}_1$, if $U_2 < C_{n_1,n_2,p}$; where $C_{n_1,n_2,p}$ are tabulated coefficients and p is the p-value.

Its application to the problem at hand is as follows: if the p-value is $p < 0.05$, we accept the alternative hypothesis of the median of the model i is bigger than the median of the model j H_1: $\mathrm{Med_j} > \mathrm{Med_i}$ for a confidence level of 95% (transitivity is self-evident, once model i drops below model j, and j below k, i ranks below k).

A clear conclusion is that the worst model is the purely Newtonian rotation curve based on visible matter, where the computed p-values with respect to the other models are all less than $p < 2.2 \times 10^{-16}$, rejecting the null hypothesis, and making it significantly the worst. This is very strong statistical evidence that visible matter is not sufficient to explain the measured rotation curves.

However, we are unable to rank Navarro-Frenk-White's spherical parametrization versus a finite-width uniform cylinder ($p = 0.053$), but we can say that these provide worse fits than MOND Standard ($p = 3.7 \times 10^{-6}$ and $p = 0.0056$, respectively). In turn MOND Standard is below MOND Simple ($p = 0.011$), and this one in turn concedes to the spherical pseudoisothermal parametrization ($p = 0.00083$). The Woods-Saxon cylinder lies above this in fit quality ($p = 9.07 \times 10^{-06}$), but below Einasto's spherical one ($p = 0.0065$), which finally is trumped by the generalized logarithmic potential ($p = 1.8 \times 10^{-07}$), a cylindrical parametrization.

With these tests completed, we obtain the classification in Table II, and notice that spherical and cylindrical parametrizations are interspersed.

We provide, in the Supplemental Material [56] to this article, eight data files `chipart1.dat` through `chipart8.dat` that list, for each galaxy (along a column), the $\chi^2/d.o.f.$ with a row for each model (the last two provide the physical model parameter $\alpha \pm \Delta\alpha$ for the best fit logarithmic potential model). The reader can find therein that occasionally there are ties or close ties for certain galaxy-model pairs. And even statistically speaking, after running over all the fittable galaxy curves, as shown in Table II, some of the models cannot be distinguished pairwise. Only a coarse ordering appears, which is what the table displays.

As an aside, given that the generalized logarithmic potential seems to provide the best fit, it is interesting to extract from the fitted galaxy sample the distribution of its parameter α in Eq. (30) and its attending uncertainty. For this extraction we add the mild requirement (that only exclude two of the sampled galaxies, NGC4085 and

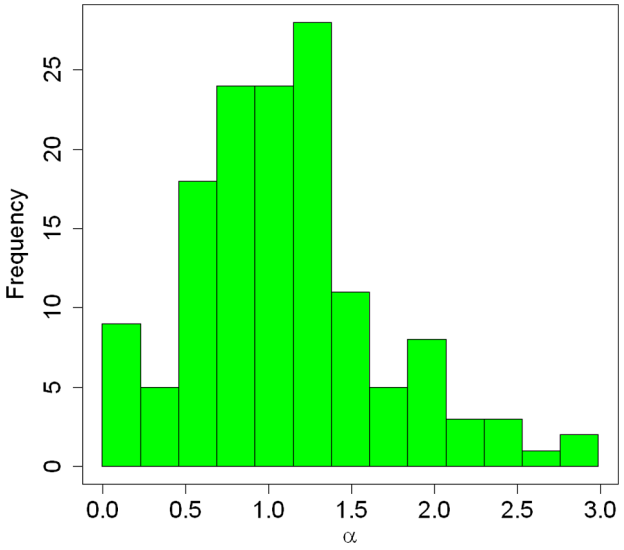

FIG. 13. Histogram of the distribution of the parameter α in Eq. (30), for the generalized logarithmic potential (very similar to that outside a cylindrical source of constant density for large r), the one that best describes the galaxy database (Table II). We have excluded a few extreme (outlier) values, not shown, from the fit. The distribution is quite peaked, and yields $\alpha = 0.456 \pm 0.003$.

UGC06787) that $\Delta\alpha$ is computable and different from 0, leaving a subset of 162 SPARC galaxies for the fit.

The distribution of α is shown in the histogram of Fig. 13: not included there are those extreme values that can be tagged as outliers. These are characterized in terms of the ith quartile Q_i and the interquartile range IQR by the conditions

$$\alpha < Q_1 - 1.5 \quad \text{IQR} = -0.78$$
$$\alpha > Q_3 + 1.5 \quad \text{IQR} = 3.3. \tag{37}$$

The resulting 162-galaxy population's "central" value for the variable $\bar{\alpha}$ and its uncertainty $\Delta\alpha$ is obtained by minimizing the statistical estimator

$$\chi^2 = \sum_{i=1}^{N} \frac{[\alpha_i^{\text{fit}} - \alpha]^2}{\Delta\alpha_i^{\text{fit}\,2}}. \tag{38}$$

The outcome is $\bar{\alpha} \pm \Delta\alpha = 0.456 \pm 0.003$.

Comparing it with Fig. 10 we see that this small value of α implies that the mass density of the cylindrical DM halo would have a very pronounced peak at $r \sim 0$ (a central filament-like structure, analogous to the "cusp" of spherical simulations), suggesting that the DM particles are heavy or strongly interacting (see discussion above Fig. 10 in Sec. II B 2 c).

As seen also in Fig. 12, we find that both cylindrical geometries and spherical geometries can account for the $V(r)$ rotation curve, and that the deciding factor, for relatively simple models, is the number of parameters that allow a better χ^2.

To gain closer understanding we wish to examine intermediate geometries between the extreme spherical and cylindrical one with varying prolateness, and even allow the fits to eventually produce the opposite, oblate DM distributions when necessary.

The systematic way to address this problem is to employ a multipole expansion. This we describe in the next two sections. In Sec. III we are going to directly expand the potential shape and use the resulting coefficients, that are expressible in terms of the underlying mass-density distribution. In Sec. IV we will instead expand the density and compute the potential therefrom. The two methods have different systematics, but yield similar results.

III. MULTIPOLE ANALYSIS OF THE GRAVITATIONAL DM HALO POTENTIAL

In this section we perform a direct multipole expansion of the potential; this is to avoid bias by choosing one particular density distribution as function of the radial-like scale. We will use it to fit the galactic rotation curves of SPARC's database assuming an ellipsoidal shape of the haloes (see Fig. 14). Then, we will obtain the degree of ellipticity that these objects present, with the notation of Table III employed throughout.

The gravitational potential generated at point $\mathbf{r}$ by an ellipsoidal density distribution can be obtained as an integral over the density,

$$\Phi(\mathbf{r}) = -G \int d^3r' \frac{\rho(\mathbf{r}')}{|\mathbf{r} - \mathbf{r}'|}. \tag{39}$$

Because of the lack of spherical symmetry of the mass distribution, the "outer" layers at $|r'| > |r|$ contribute. To systematically treat this deviation from sphericity, we will deploy a multipole expansion in terms of $Y_l^m(\theta, \phi)$ [57] demanding that the expansion coefficients encode the residual symmetries of the ellipsoid. These are the axial

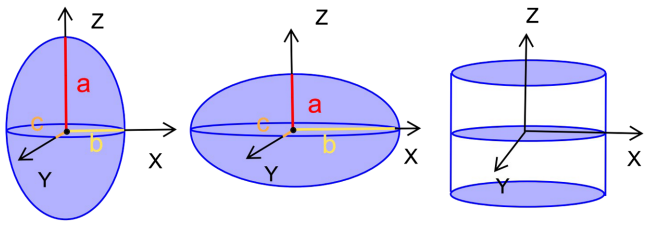

FIG. 14. Variables used to describe typical elongated halo geometries. Left: prolate ellipsoidal mass distribution (interpolating between spherical and cylindrical) with a the major and b, c the minor semiaxes. Middle: ellipsoidal oblate mass distribution with a the minor and b, c the major semiaxes. Right: cylindrical distribution as the extreme case. The triaxiality is taken as zero as in all the manuscript.

symmetry around the OZ-axis (that fixes the second multipole index as $m = 0$) and the reflection-symmetry on the galactic plane (that restricts l to be even). Thus,

$$\Phi(\mathbf{r}) = -G \sum_{l \text{ even}, m=0} P_{lm}(\theta, \phi) \left[\frac{I_{l0}(r)}{r^{l+1}} + r^l Q_{l\geq 2, m=0}(r) \right]. \tag{40}$$

Here I_{lm} and Q_{lm} represent the coefficients of the internal- and external-layer contributions, respectively, obtained upon integrating the density in the respective domain over the corresponding Legendre polynomials $P_{l0}(\theta) = \sqrt{4\pi/(2l+1)} Y_{l0}(\theta)$,

$$I_{l0}(r > r') = \int d\Omega' \int_0^r dr' (r')^{l+2} \rho(\mathbf{r}') P_l(\theta') \tag{41}$$

$$Q_{l0}(r < r') = \int d\Omega' \int_r^\infty dr' (r')^{1-l} \rho(\mathbf{r}') P_l(\theta'). \tag{42}$$

(The upper integration limit in Q_{l0} is of course a maximum R when implemented on a computer; the external, spherical Q_{00} contributes an upper integration-limit dependent constant (respect to the angles and inner radii) j to the potential as per Gauss's theorem.)

We extend the multipolar expansion to the monopolar $l = 0$, quadrupolar $l = 2$, hexadecapolar $l = 4$, and 64-polar $l = 6$ terms. We then obtain the rotation velocity from the resulting potential in Eq. (40) as

$$V^2 = -r \frac{\partial \Phi(\mathbf{r})}{\partial r}. \tag{43}$$

To examine the geometry with this analysis, independent of that in Sec. II, we need to adopt any one of the reasonable halo density profiles as function of the distance scale. We have chosen two of the simplest models: the first is simply a two-parameter step distribution

$$\rho(r, \theta) = \rho_0 \Theta(R(\theta) - r) \tag{44}$$

with a constant inner density that suddenly drops to zero outside of $R(\theta)$, which we take as the ellipsoid given by Eq. (45) below

$$R(\theta) = \frac{1}{\sqrt{\frac{\sin^2\theta}{b^2} + \frac{\cos^2\theta}{a^2}}}. \tag{45}$$

As a second parametrization, we have chosen a Woods-Saxon density profile, a well studied function that is used in several fields of physics to represent a core followed by a decrease whose value decays away from the gravitational source in a parametrically controlled way (it is also functionally identical to the Fermi-Dirac distribution),

TABLE III. Convention for the relative size of the characteristic lengths a, b, c along the three principal axes of an ellipsoidal halo. See Fig. 14.

Halo	Axes relation
Prolate	$a > b \simeq c$
Oblate	$a < b \simeq c$
Triaxial	$a > b > c$

$$\rho_{W-S}(r, \theta) = \frac{\rho_0}{1 + e^{(r - R(\theta))/a_0}}. \tag{46}$$

Each of these two has been employed with each of the first orders of the expansion in Eq. (40) up to $l = 6$, and then also with a purely cylindrical distribution to yield a total of ten different parametrizations listed in Table IV.

Each galaxy $j = 1, \ldots 153$ (those with acceptable rotation curves with enough data points and known behavior near $r = 0$, see discarded galaxies in Table XIII, and sufficiently many measured points to be usable for this analysis) assigns each parametrization $i = 1, \ldots, 10$ a rank R_{ij} based on ordering the fit χ^2 from smaller to larger values. The rank can take values from 1 to 10, where 1 describes the best parametrization. We can obtain a global rank for each approach calculating the mean value $\bar{R}_i = \frac{1}{N} \sum_j^m R_{ij}$ or the median of the individual galaxy ranks. These mean and median are also listed in Table IV.

As the table shows, a purely cylindrical potential (and thus, the entailed dark matter distribution) and those with higher multipoles (distorting the spherical symmetry) seem to perform better than those nearly spherical shapes.

The full histogram distribution from which the table is extracted is also shown in Fig. 15. It is patent to the eye that the best fitting angular distributions are those with a

TABLE IV. Angular-dependence parametrization, density profile as function of the distance to the galactic center, number of fit parameters, median value (with uncertainty), and mean value (with standard deviation). (This analysis is based on 153 of the 175 galaxies; the excluded ones have less than 5 measured points or notably poorer data quality.).

Angular shape	Density profile	$N_{\text{F.P.}}$	Median $\pm$ MAD	$\bar{R}_i \pm \sigma$
Cylinder	Woods-Saxon	3	4.0 ± 2.0	4.1 ± 2.4
Cylinder	Constant	2	4.0 ± 2.7	4.5 ± 3.2
$l = 0, 2, 4$	Woods-Saxon	4	5.0 ± 2.2	4.8 ± 2.4
$l = 0, 2, 4$	Constant	3	5.0 ± 2.7	5.4 ± 3.0
$l = 0, 2, 4, 6$	Woods-Saxon	4	6.0 ± 2.3	5.4 ± 2.6
$l = 0, 2, 4, 6$	Constant	3	6.0 ± 2.5	5.8 ± 2.9
$l = 0, 2$	Woods-Saxon	4	6.0 ± 2.2	5.9 ± 2.5
$l = 0, 2$	Constant	3	6.0 ± 2.3	5.9 ± 2.7
$l = 0$	Constant	3	6.0 ± 2.4	5.7 ± 2.7
$l = 0$	Woods-Saxon	4	9.0 ± 2.3	7.7 ± 2.6

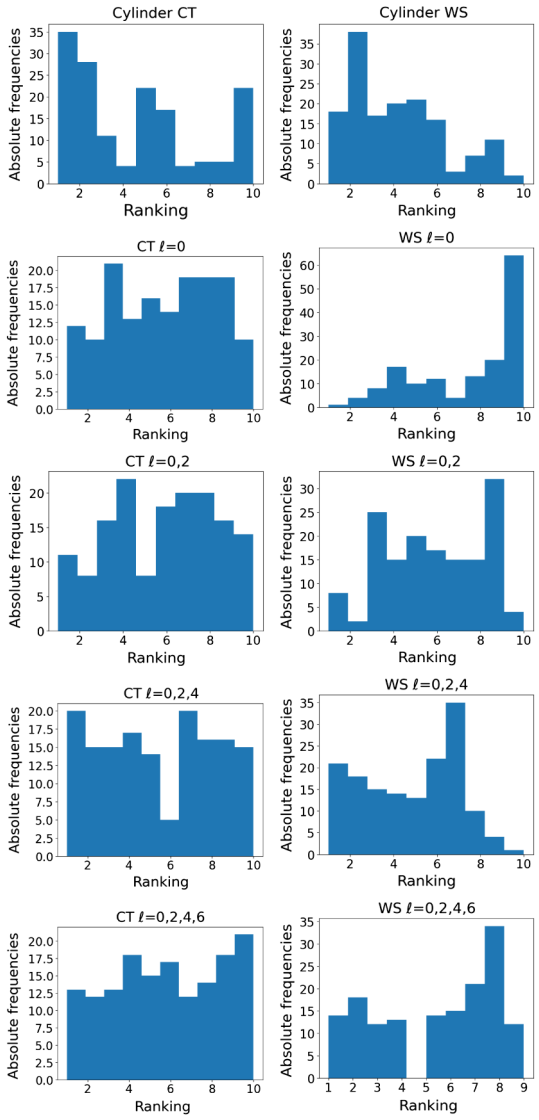

FIG. 15. Histograms exposing the distribution of $\chi^2/N_{\rm F}$ rankings for each parametrization in Table IV (mapping out a multipole expansion of the potential). The OY axis is the number of galaxies that classify the calculation in each box in the corresponding bin. Both spherically-symmetric models ($l=0$, second row) are ranked in the worst tier (8, 9, or 10). On the other hand, the dispersion difficults a successful extraction of the higher $l=6$ multipoles, so we concentrate on $l=0$, 2 and $l=0,2,4$. The cylindrical fits (first row) are rather good too.

filamentary distribution of dark matter (cylindrical distribution).

Figure 16 shows the shape of the typical theoretical rotation curves corresponding to these histograms. On the top plot we see that a significant contribution to a flat rotation curve comes from the hexadecapolar multipole term of the potential, $l=4$, which elevates the rotation curve at larger radii. This must be the reason why the $l=0,2,4$ parametrization provides better fits that the $l=0,2$ and $l=0,2,4,6$ parametrizations, as seen in Table IV. From $l=4$ to $l=6$ the difference is small

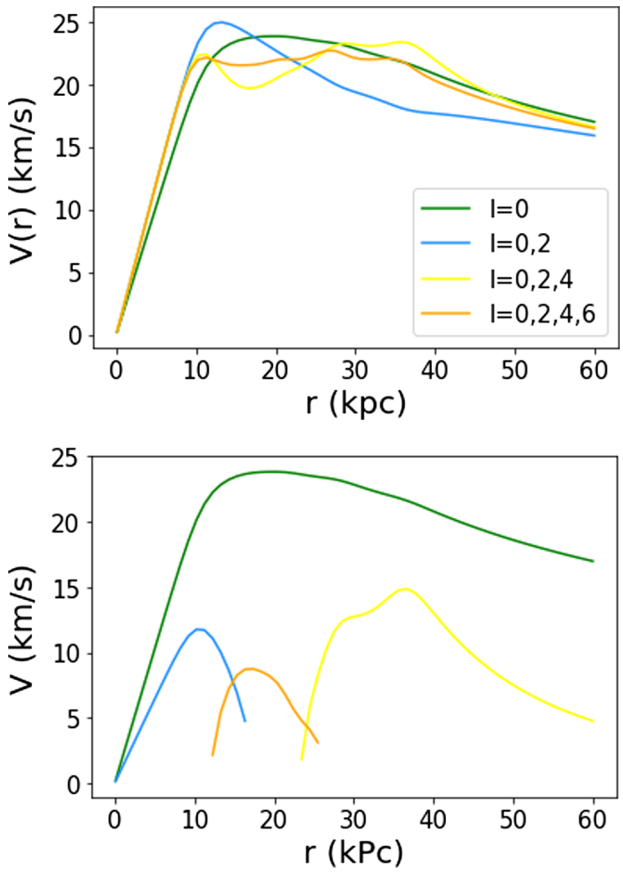

FIG. 16. Separate contributions to the rotation curve $V(r)$ in a multipole analysis. They are added up in the top plot, while separately shown on the bottom one. Identifiable in that bottom plot from left to right, shown are the multipoles $v_{l=0}$ (green), $v_{l=2}$ (blue), $v_{l=6}$ (orange), and $v_{l=4}$ (yellow) using the Wood-Saxon density profile with a prolate DM halo of semiaxes length $a=40$ kpc, $b=c=10$ kpc.

and the fit fluctuates, so not much is gained by the additional multipole.

In galaxies where the rotation curve lies flat from the center $r=0$ on, such as UGC03546 in Fig. 17 or those that become constant at larger distances such as DDO064, higher order multipoles will be needed to fit the rotation curve. The worst fits are obtained with a spherical distribution of dark matter. We expect this to be a generic feature of most DM density profiles excepting those that are near the isothermal one, $\rho\propto 1/r^2$ (in this case, an r-independent v falls of from Kepler's 3rd law in orbital equilibrium).

A. Comments on the fitting methodology

In the first place, the `iminuit` minimization of $\chi^2/N_{d.o.f.}$ occasionally becomes stuck in local minima; as a corrective measure we have visually examined each rotation curve fit and hand-restarted the minimizer to explore other parameter regions.

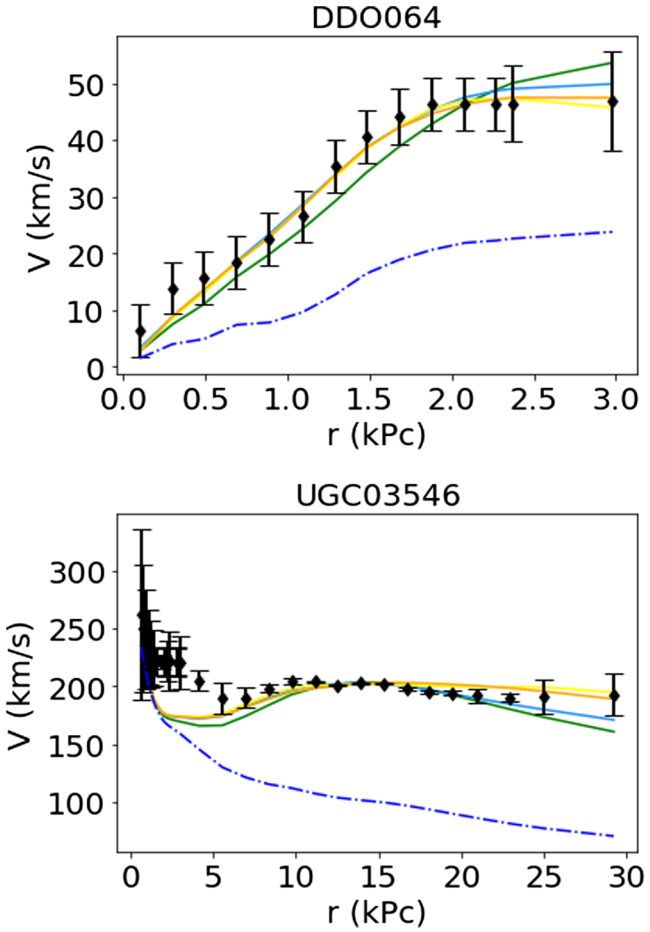

FIG. 17. Fit to the rotation curves $V(r)$ for two galaxies with different profiles using the multipole expansion of DM potential, Eq. (40). SPARC data from [3]. The dotted line (blue) is for the V_{BA} rotation curve, the solid green one is for the $l = 0$ fit, the solid blue line includes both $l = 0, 2$, the yellow one is for the $l = 0, 2, 4$ fit and finally the orange line is for the $l = 0, 2, 4, 6$ fit.

Second, in rotation curves with very flat profiles, the dark matter modeled in this section is not always enough to explain the behavior of $V(r)$ near the galactic center. This is exemplified by the UGC03546 galaxy in Fig. 17 and may have to do with the old core-cusp problem that we are not numerically studying in this work.

Fits that use as a density profile the Wood-Saxon function adapt better to the shape of the velocity profile in the cases where the velocity increases with r and then becomes constant at large r. As an example, see galaxy DDO064 in Fig. 17.

IV. MULTIPOLE EXPANSION OF THE DM DENSITY

In this section, to explore the systematics, instead of directly performing a multipolar expansion of the potential, we expand the dark matter density and afterwards calculate the potential. The method followed is akin to the one used in nuclear physics for the study of collective vibrational shell models [58,59] where it is used to study the deformation of certain nuclei and also heavy ion collisions [60].

We start again from a Woods-Saxon density as in Eq. (46)

$$\rho_{W-S}(r,\theta,\phi) = \frac{\rho_0}{1+e^{(r-R(\theta,\phi))/a_0}}, \tag{47}$$

the difference now being that instead of employing Eq. (45) to compute the gravitational potential and then expanding $\Phi(r,\theta)$, we now expand this density distribution itself.

The same procedure will be applied to the (two-parameter) step density distribution in Eq. (44). We expand this $R(\theta,\phi)$ in terms of spherical harmonics, noticing that with $m = 0$ they are real, and the β coefficients are also real numbers,

$$R(\theta) = R_0 \cdot \left[1 + \sum_{l=1}^{\infty} \beta_{l0} Y_{l0}(\theta)\right]. \tag{48}$$

We now apply the symmetry conditions of Sec. III, and the only terms left will then be those with even l and $m = 0$. We will once more truncate the expansion including only the monopolar, quadrupolar, and hexadecapolar terms, leaving two β deformation parameters:

$$R(\theta) = R_0 \cdot [1 + \beta_{20} Y_{20}(\theta) + \beta_{40} Y_{40}(\theta)]. \tag{49}$$

The first one, β_{20}, is related to the elongation of the ellipsoid of revolution that represents the shape of the halo, as can be seen for a solid body (the limit in which the Woods-Saxon edge is set to zero) for which it takes the form

$$\beta_{20} = \sqrt{\frac{16\pi}{45}} \frac{1-s^2}{1+s^2}. \tag{50}$$

The ellipticity ratio $s = b/a \in (0,\infty)$ carries the information on the quadrupole deformation of the halo. According to Eq. (39) the gravitational potential is then calculable as

$$\Phi(r,\theta,\phi) = -G \int d\Omega' \int_0^{\infty} dr' \frac{r'^2 \rho_{W-S}(r',\theta',\phi')}{|r-r'|}, \tag{51}$$

the denominator in this equation (that yields the static Green function), is, in spherical coordinates,

$$|r-r'| = \sqrt{r^2 + r'^2 - 2rr'(s_\theta c_\phi s_{\theta'} c_{\theta'} + s_\theta s_\phi s_{\theta'} s_{\phi'} + c_\theta c_{\theta'})}. \tag{52}$$

To calculate the rotation curve, it suffices to consider the motion in the plane $\theta = \pi/2$, and $\phi = 0$ can be taken given the remaining cylindrical symmetry.

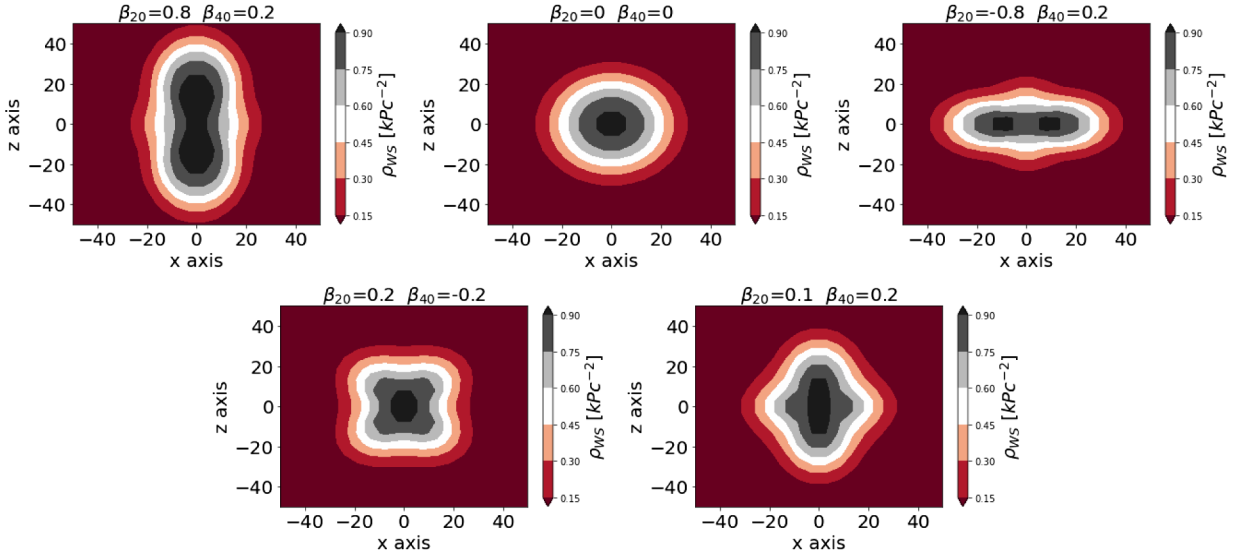

FIG. 18. Shapes of the components of a halo that are obtained upon expanding the Woods-Saxon density profile in Eq. (47) for a halo with $a_0 = 6$, $R_0 = 20$ (units in kpc). Clockwise from the top left we find prolate (P), spherical (S), oblate (O), amphora (A), and teacup (T) shapes, all axisymmetric.

For comparison with the spherical harmonic expansion of the potential, we will employ in parallel an "unexpanded" parametrization which is the one given in Eq. (51) but with the halo edge as defined in the density profile from Eq. (45).

We can expand Eq. (48) to higher orders, and have done so for exploratory purposes. But for large values of higher β coefficients, the surface of the halo can oscillate due to the intricate shape of the Legendre polynomials. To avoid it we need to impose a condition of convexity, best expressed in Cartesian coordinates as $z''(x) < 0$ (because the figure has azimuthal symmetry, $x = r_\perp$ can be any direction in the XY plane). This restriction binds the values that the parameters β_{l0} can take as $|\beta_{20}| \leq 1$, $|\beta_{40}| \leq 0.3$, the same as higher multipole orders. With these figures we have allowed, as an exercise, somewhat larger values than those given a perfectly convex body, as shown in Fig. 18. Shaving $|\beta_{20}|$ to be under 0.7, $|\beta_{40}|$ to be below 0.2, and the higher ones to be at most 0.1, eliminates the concavities of the resulting figures if needed.

We can classify the shape of the resulting haloes in five classes, as seen in the figure, which we have tagged as oblate (O), prolate (P), spherical (S), teacuplike (T), and amphoralike (A).

The fit with the most parameters is that with $l = 0, 2, 4$ (that depends on ρ_0, the central density, a_0, the skin-thickness parameter, R_0, the halo width in the equatorial plane, and the intensities $\beta_{20}(s)$ and β_{40}). The number of

TABLE V. Goodness of fit in several approaches: two multipole expansions, an unexpanded ellipsoidal model and a model with perfect cylindrical shape. Given are each model's angular shape and density profile, the type of halo edge, the number of fit parameters, and both the median and the mean values of χ^2/d.o.f. with their respective deviations: this roughly orders the models from top to bottom according to efficiency of the data description.

Angular shape	Density profile	Parametrization	$N_{\text{F.P.}}$	Median $\pm$ MAD	$\overline{R}_i \pm \sigma$
Cylinder	Woods-Saxon	R_0	3	2.0 ± 1.3	2.8 ± 1.6
Cylinder	Constant	R_0	2	2.0 ± 2.2	3.1 ± 2.5
Unexpanded	Woods-Saxon	$R(\theta, a, b)$	4	3.0 ± 2.0	3.9 ± 2.4
$l = 0, 2, 4$	Woods-Saxon	$R(\theta, s, \beta_{40}, R_0)$	5	5.0 ± 1.8	5.7 ± 2.2
$l = 0, 2$	Constant	$R(\theta, s, R_0)$	3	5.0 ± 1.9	4.9 ± 2.2
Unexpanded	Constant	$R(\theta, a, b)$	3	6.0 ± 1.9	5.9 ± 2.2
$l = 0$	Constant	$R(\theta, R_0)$	2	6.0 ± 1.9	5.9 ± 2.4
$l = 0, 2, 4$	Constant	$R(\theta, s, \beta_{40}, R_0)$	4	7.0 ± 2.0	6.9 ± 2.5
$l = 0$	Woods-Saxon	$R(\theta, R_0)$	3	9.0 ± 1.4	8.3 ± 1.8
$l = 0, 2$	Woods-Saxon	$R(\theta, s, R_0)$	4	9.0 ± 2.2	7.6 ± 2.6

galaxies that have at least five data points so that a $\chi^2/d.o.f.$ makes sense is 157; the other 18 galaxies in the SPARC file are discarded for this fit. We must also discard a further four galaxies with unacceptable rotation curves for this exercise: see the explanation in Table XIII). Finally, we perform the fits over the remaining 153 galaxies of SPARC's database.

From the fit results within the allowed multipole parameter range, the ellipticity that we deduce from Eq. (50) shows large variations, with values $s \in [0.16, 6.25]$. We also compare the fits obtained from multipole expansion parametrizations with those of a purely cylindrically shaped parametrization and an unexpanded ellipsoidal parametrizations, using either of the hard density, Eq. (47), or soft density, Eq. (44), profiles for the R defined in Eq. (45).

In this section we study ten parametrizations; therefore the ranking values range from 1 to 10, with 1 being assigned to the best fit.

As Table V shows, a potential that is purely cylindrical (as thus is the entailed dark matter distribution) and those with higher multipoles (distorting the spherical symmetry) perform better than those with nearly spherical shapes. In particular, the unexpanded ellipsoidal parametrization seems to provide good fits. We will strive to analyze the ellipticity that is obtained from this parametrization in the next Sec. V, to understand whether the good fits are indeed due to elongated shapes.

The full histogram distribution from which the table is extracted is also shown in Fig. 19. It is again noticeable that the best fitting angular distributions are those with an elongated distribution of dark matter (either cylindrical distribution or those with higher order terms in the expansion).

We notice that the quadrupolar and hexadecapolar parametrizations alternate in quality depending on whether the hard step or the soft density profile is used, showing that there is not very large sensitivity to terms above the quadrupolar.

In Fig. 20 we see that a remarkable contribution to a flat rotation curve comes however from the hexadecapolar multipole term $l = 4$, as it lowers the rotation curve at the beginning of the flat region and, thus, the curve seems to become constant. Still, the $l = 0, 2$ parametrization is similar to that with $l = 0, 2, 4$, and differs only at the beginning of the flat region.

Also seen is the spherical $l = 0$ parametrization: it falls with the characteristic $1/\sqrt{r}$ after a certain radius R_0. Lastly, the unexpanded shape, when prolate, seems to yield a rotation curve similar to that of the higher multipole parametrizations.

In all, the expansions with $l = 0, 2$ and $l = 0, 2, 4$ provide similar fits, with $l = 0$ slightly worst. The unexpanded ellipsoid seems to be the most successful model in this family.

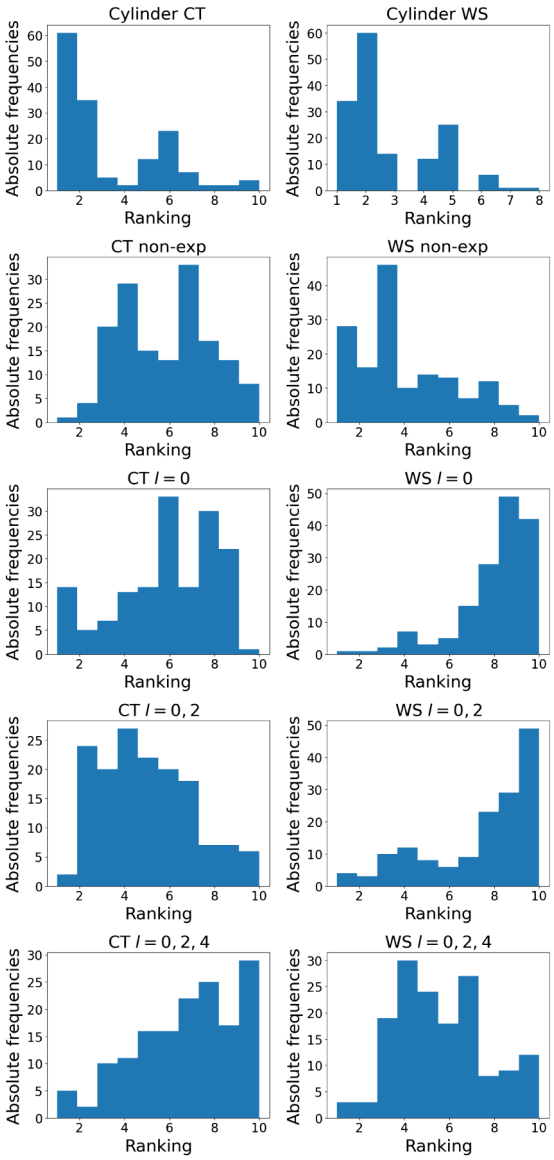

FIG. 19. Histograms exposing the distribution of χ^2/N_F rankings for each parametrization in Table V (mapping out a multipole expansion of the density profile). The OY axis is the number of galaxies that classify the calculation in each box in the corresponding bin. The behavior of the expansion parametrizations is different for both density profiles, soft density profiles (WS = Woods-Saxon) work better for higher multipole orders ($l = 0, 2, 4$), whereas hard density profiles (CT = constant density up to the edge) work better for $l = 0, 2$. Nonetheless, spherical shapes $l = 0$ do not provide good fits in any of the cases. On the other hand, unexpanded profiles that allow for an ellipsoidal and/or spherical halo seem to give rather good fits, topped however by the cylindrical-source fits (first row) that seem to be best.

In galaxies where the rotation curve is flat from the outset at $r = 0$, such as UGC03546 seen shortly in Fig. 17, or those that become constant at larger radii such as DDO064, higher order multipoles will be needed to fit the rotation curve. The worst fits are obtained with a

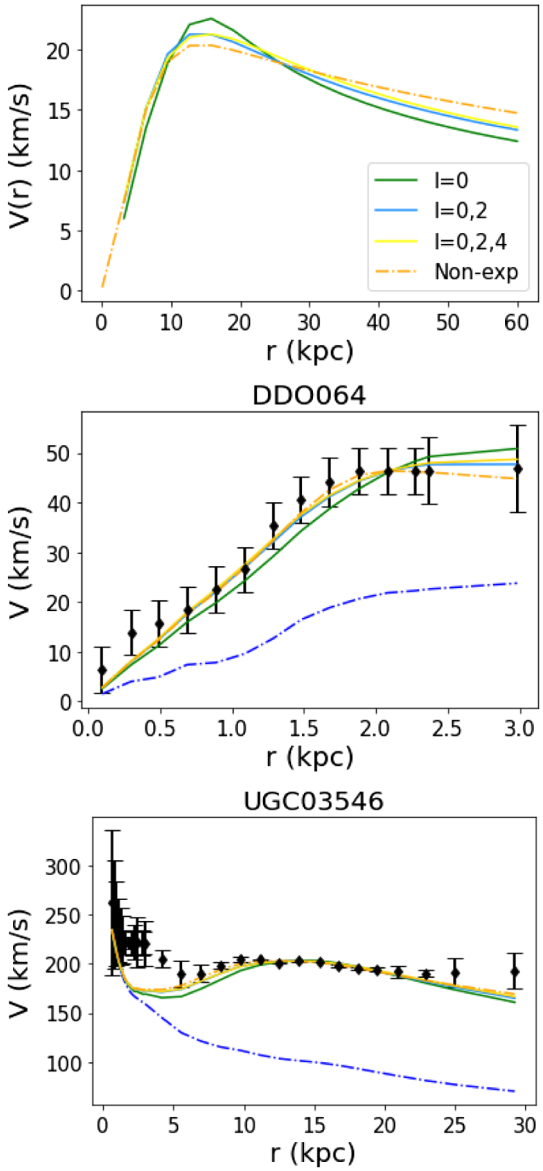

FIG. 20. Top: contribution of the multipoles of $\rho(r,\theta)$ in Eq. (49) to the rotation curve. Reading from bottom to top at large radius they are ($v_{l=0}$ in green, $v_{l=0,2}$ for blue and $v_{l=0,2,4}$ the yellow line). The dot-dashed (orange) line represents the unexpanded parametrization to $V(r)$ using the softer Wood-Saxon density profile for a DM halo with semiaxes $a = 50$, $b = c = 8$ in kpc ($s = 0.16$ and $\beta_{04} = -0.3$). Middle and bottom: fit to the rotation curve for two problematic galaxies with $V(r)$ profiles different from the standard shape. The additional dashed-dotted lowest line (blue) corresponds to the V_{BA} visible matter rotation curve. The few nonconforming galaxies of this type are the ones that make the fitting procedure more difficult.

spherical distribution of dark matter. As in the last section, we expect this to be a generic feature of most DM density profiles excepting those that are near the isothermal one.

From fits like those in Fig. 20 we can obtain the relation between the major and minor axes using Eq. (50). According to the values of β_{20} and β_{40} the fits will fall in one of the five categories (P, O, S, T, A). The haloes that we fit in the end, will range from spherical $s = c/a = 1$ to very prolate haloes $s = c/a = 0$. Below, in Fig. 28 we will see that for these models the trend is for the halo to become prolate rather than spherical, although there will also be some haloes that turn out oblate.

We finally note that many of the galaxies push the parameters to the boundaries of their allowed interval. Particularly those where $V(r)$ is very flat (Rubin's observation) push them to the most elongated shape allowed $s \to 0.16$, with $\beta_{40} \to -0.3$ also at the limit of distortion that we allow.

V. STATISTICAL EXTRACTION OF THE HALO ELLIPTICITY

We now turn to the statistical characterization of the ellipticity s over the sample of galaxies in SPARC.

A. Definite model: Exponential ellipsoid parameterization

In this subsection we report a model-dependent extraction of the ellipticity from a simple, generic exponential density distribution. We choose it to have its surfaces of constant density be ellipsoids with revolution symmetry [$b = c$, that is, we do not consider triaxiality that does not play a role in $V(r)$] satisfying

$$\frac{x^2 + y^2}{c^2} + \frac{z^2}{a^2} = \text{const} \tag{53}$$

for which the ellipticity is trivial to assess. In cylindrical coordinates, with $r = r_\perp \equiv \sqrt{x^2 + y^2}$, an apt choice is then

$$\rho(r,z) = \rho_0 e^{-\frac{1}{b}\sqrt{r^2 + (b/c)^2 z^2}}. \tag{54}$$

Introducing once more the ellipticity parameter $s = c/a$ and redefining $R := b$ we have

$$\rho(r,z) = \rho_0 e^{-\frac{1}{R}\sqrt{r^2 + s^2 z^2}}. \tag{55}$$

This density profile has four degrees of freedom: the "hidden" power law of the argument of the exponential, which is fixed to 1, and the three manifestly free parameters ρ_0, R and s.

There is no analytical expression for the gravitational field of this density profile, and thus we calculate it numerically from the general expression

$$\mathbf{g}(\mathbf{x}) = -G \int d^3x' \rho(\mathbf{x}') \frac{\mathbf{x} - \mathbf{x}'}{|\mathbf{x} - \mathbf{x}'|^3}. \tag{56}$$

Since the spiral-galaxy rotation curve $V(r_\perp)$ is measured on the galactic plane, we only need the radial component $g_\perp$, which in spherical coordinates can be written as

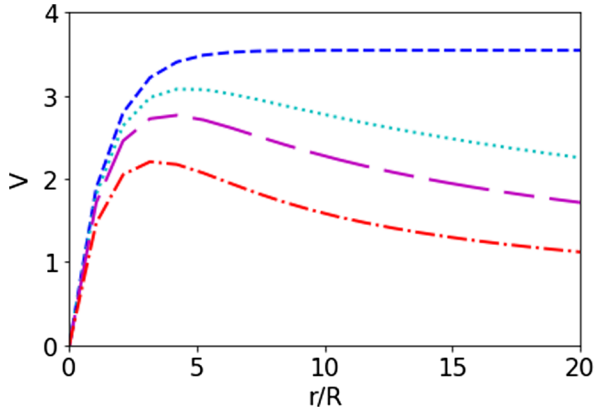

FIG. 21. $V(r)$ rotation curve for the ellipsoidal dark matter distribution of Eq. (55). The extreme values are $s = 1$ (dashed-dotted line, red) corresponding to a spherical distribution, at the bottom, and $s = 0$ (dashed line, dark blue), the limit of a cylindrical distribution, at the top. Also given are intermediate values $s = 0.4$ (dashes of alternating size, purple) and $s = 0.2$ (dotted line, light blue).

$$g_r(r) = \int d^3x' \frac{-G\rho(\mathbf{r}') \cdot (r - r' \sin\theta' \cos\phi')}{(r^2 + r'^2 - 2rr' \sin\theta' \cos\phi')^{3/2}}. \quad (57)$$

Finally, we obtain the rotation curve through Eq. (3). Adequately normalized ones are plotted in Fig. 21 for different values of s. The dashed line at the bottom corresponds to $s = 1$: the source is spherically symmetric and $V(r)$ decreases for $r/R > 5$ as per Kepler's 3rd law. As we give s smaller values, $V(r)$ becomes less slanted, and when $s = 0$ (the top curve) we see the characteristic flattening of cylindrical sources. Thus, we have an appropriate interpolating model between cylindrical and spherical geometries as function of one parameter.

By fitting the same subset of rotation curves used in Sec. II we can obtain the value of s as well as its $1-\sigma$ uncertainty. Minimization with `iminuit` becomes slow due to the triple integration in Eq. (57). To reduce running time it is convenient to use an adapted limit of integration for the radial variable, $r' \in [0, r + 10R]$. We are satisfied with relative numerical errors below the 10% level that are under the typical statistical uncertainty in the s ellipticity parameter: δ_V reaches its maximum for $s = 0$ (cylindrical source) as $\delta_V = 0.05$ for $r = 10R$ and $\delta_V = 0.09$ for $r = 20R$, increasing with radius.

In Fig. 22 we show a histogram of $\log s$, based on the logarithmic scatterplot of Fig. 23 with the s values obtained for each individual galaxy.

A supermajority of galaxy DM haloes is then prolate, and lies below the horizontal bar (blue) at $s = 1$ in the figure. There are however 29 galaxies with $s > 1$ at $1-\sigma$ level.

The resulting 164-galaxy population's "central" value for the ellipticity variable s and its uncertainty Δs, within this exponential parametrization of the radial dependence, is obtained by minimizing the statistical estimator

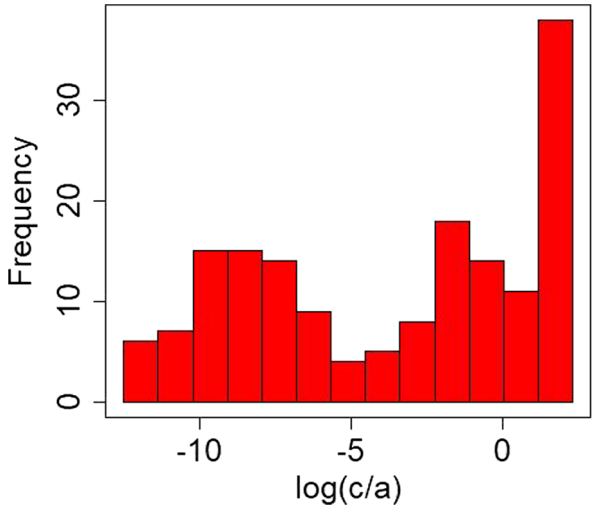

FIG. 22. Histogram of the distribution of $\log c/a$ for the exponential ellipsoid parametrization. It is clear that the data suggests many very prolate DM haloes with negative log, whereas those that come out oblate are not very much so, but stay relatively near the spherical shape.

$$\chi^2 = \sum_{i=1}^{N} \frac{[s_i^{\text{fit}} - s]^2}{\Delta s_i^{\text{fit}\,2}}. \quad (58)$$

This should not be applied blindly. Careful analysis shows that a very few galaxies with very small uncertainty band in their own ellipticity have a disproportionate effect on the central value of the entire set. This may be a reason why earlier literature found contradictory results.

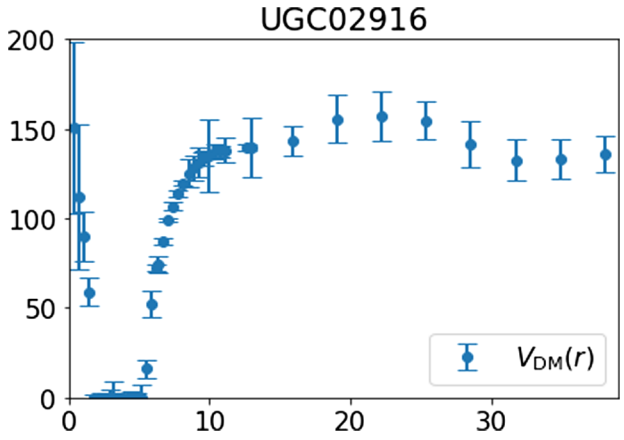

FIG. 23. (Pseudo-) data V_{DM} after subtracting SPARC's visible matter component off the UGC02916 rotation curve. This galaxy is an example where an oblate DM distribution is favored by the fit, with an incredibly small χ^2 that pulls the global fit of the entire database. But notice the pronounced minimum at few kpc that makes us doubt that the SPARC extraction of the visible matter components, leaving this squared velocity to be explained by dark matter, is totally reliable. Notice in particular that at large radii $V(r)$ flattens to a constant, as typical spiral galaxies do, suggesting prolateness in the end. It is the small r part, very impacted by the visible matter, that is driving the fit.

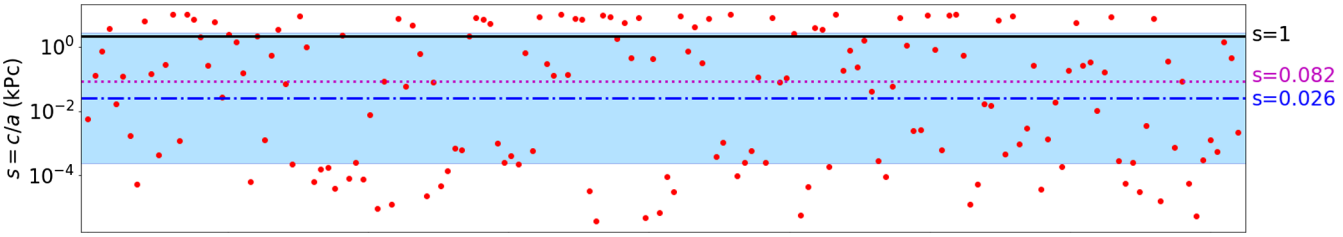

FIG. 24. Ellipticity ratio $s = c/a$ from fitting an exponential ellipsoid parametrization to the subset of rotation curves from the SPARC database selected in Sec. V A [3]. Most galaxies lie underneath the $s = 1$ solid line (black), suggesting prolate haloes. The dotted line (purple) is the median of the distribution, while the dashed line and the shadowed region (blue) denotes the geometric mean and its confidence interval.

For example, UGC02916 tends to prefer an oblate halo and seems to yield an amazingly precise ellipticity of $s = 2.63398(1)$. Due to such unbelievable goodness of fit, this one galaxy almost by itself pulls the central ellipticity to $\bar{s} \pm \Delta s = 2.14901(1)$, on the oblate side as it is larger than 1.

Closer examination of this one galaxy (see Fig. 24) shows that at large r the behavior of $V(r)$ is that of a typical spiral galaxy with a prolate halo, and that the $s > 1$ value is driven by the small-r dip, very suggestive of a poorly controlled visible-matter distribution.

We have individually examined the minority of galaxies that have positive $s - 1$ and suggest an oblate DM halo. Most of them have a rotation curve that is *increasing* with distance out to the farthest measured point, that is, measurements have probably not extended far out enough to see the typical settling into a flat rotation curve. A much smaller number of others fall in alternative categories (large uncertainties, very untypical behaviors such as a quick falling of $V(r)$ as a step function, etc.) and are classified in Appendix A 1.

This apparently outlier galaxy, UGC02916, belongs to the first class of the categories there defined: its pseudodata DM rotation component exhibits a pronounced oscillation at small r. Excluding this one galaxy from the analysis we immediately obtain an extremely prolate (and unreasonably accurate) value for the distribution, $s = 0.05845(2)$. Plucking off the next-to extreme galaxy, in this case a prolate one, returns the central ellipticity to order $s \simeq 0.3$; this instability of the global fit to a few galaxies is typical of statistical samples with outliers, and the correct procedure is to remove them.

Since there is some ambiguity in the point where the remotion of outliers needs to stop (several conventions are used in the literature), we have opted for iterating the process of removing one value at a time with lower uncertainty in s to obtain a sequence of central s values for a decreasing number of galaxies s_n.

We consider that the value computed is reliable when two consecutive values of s are compatible at $1 - \sigma$. This first happens after removing 32 galaxies, leading to a tentative result at 1σ of $s = 0.693 \pm 0.027$ that we have plotted in Fig. 1.

It is in carrying out this exercise when we have realized that the more revealing statistic estimator is the geometric mean, or the logarithmic average, as discussed below in Sec. VI A. Indeed, if the geometric mean of each galaxy's ellipticity is taken, $\sqrt[n]{s_1 \cdot s_2 \ldots s_n}$, it turns out to yield a very prolate value, $\exp\langle \log s \rangle = 0.026$ which amounts to the longer axis being 38 times larger than the shorter ones (on average) However, the spread is large, with a confidence interval for the variable $\log s$ that is $\log s = -3.6 \pm 4.7$ or, exponentiating, $s = [0.0002, 2.783]$. That is, there are some DM haloes that are preferably fit to truly filamentary shapes with $s \ll 1$, while a few can be somewhat oblate, like a thick pancake. On log average, it is clear that they tend to strong prolateness.

B. Extraction from the multipole expansion of the DM potential

In this subsection we quickly turn to the extraction of the ellipticity $s = c/a$ from the multipole expansion of the potential in Sec. III.

As is shown in Fig. 25, the behavior of the rotation curve varies in function of the distortion of the halo shape. In prolate haloes (violet line) $V(r) \sim$ constant when $b \leq r \leq a$ and in oblate haloes (orange line) $V(r)$ increases when $a \leq r \leq b$. However, when r is taken outside of the total distribution the rotation curve decreases $V(r) \propto 1/\sqrt{r}$, that happens when: $r > a$ in prolate types, $r > b = c$ in the oblate ones and $r > a = b = c$ in spherical haloes.

We notice that only prolate haloes are apt to explain the flat rotation curves that are seen in many galaxies. To simulate the constant velocity profile we need at least the contribution of the hexadecapolar term $l = 4$ (the yellow line in Fig. 16) to the rotation curve. The consequent addition of a higher multipole term up to $l = 6$ (the orange line in Fig. 16) should soften the velocity profile at moderate radii, as we can see in Fig. 25.

In Table VI we provide the outcome of the fits for the ellipticity $s = b/a$ of the haloes for the galaxies in SPARC's database. Be reminded that $l = 0$ corresponds to spherical haloes, when taking higher orders, flattened or

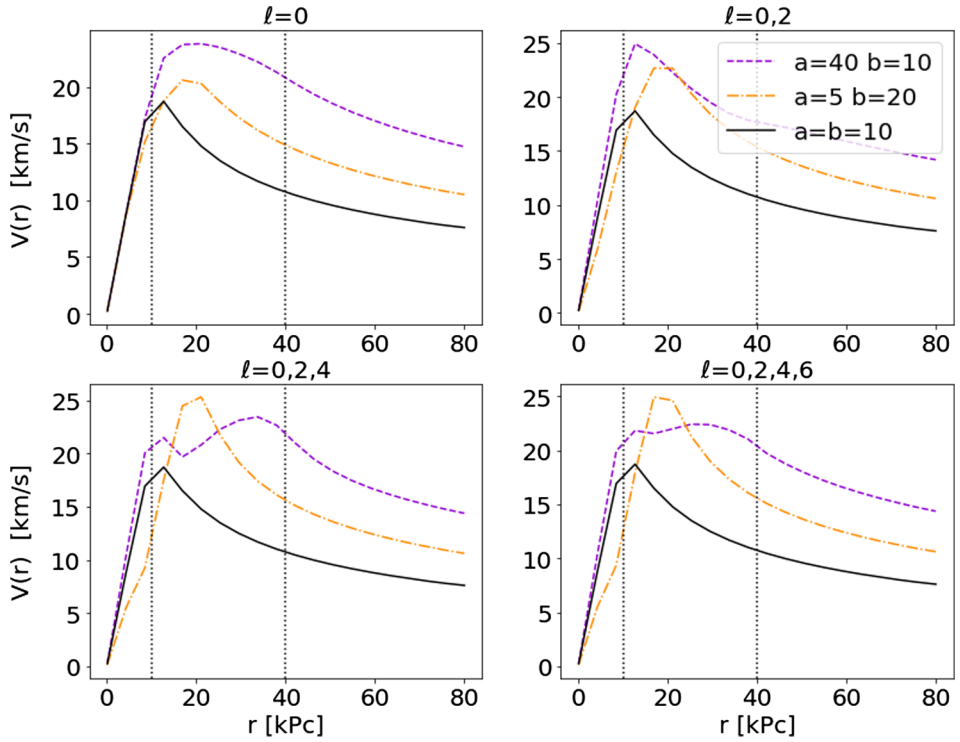

FIG. 25. Ellipticity dependence of the DM rotation curve from the multipole expansion of the potential, Eq. (40), to the indicated expansion orders: the smaller s (the more prolate the halo), the flatter the rotation curve. Solid black line: reference spherical halo (the same in all plots). Dashed-dotted line (orange): oblate halo (it falls faster after reaching the peak rotation velocity). Dashed line (purple): prolate halo ($V(r)$ falls slower after its peak).

elongated sources can be described (the quality of the respective fits was seen in Table IV and will not be repeated here).

It is clear from Table VI that the average (arithmetic mean) is quite meaningless for this variable and any biases on which galaxy is included or not can shift it from below to above 1 (prolate to oblate). The median, on the second to last column, is seen to consistently be below 1 (indicating therefore a clear preference for prolate shapes except, of course, the $l = 0$ fit that cannot but be spherical).

TABLE VI. Value of the ellipticity s of the haloes for each parametrization in Sec. III. From left to right the columns correspond to the angular-dependence parametrization, the soft or hard density profile, the median value of s, and the arithmetic mean of the s values. We give the one-sided uncertainty which is very large because of a few very oblate haloes that distort the arithmetic averaging. In consequence, the last column quotes the geometric mean, that is seen to be well below 1 in all cases. In this case, $l = 0$ does have a residual sensitivity to the halo shape through the ratio a/b on which R of Eq. (44) depends: the fit of the matter density in Table VIII below is cleaner in this respect.

Multipole	Density	MED$^{+\mathrm{MAD}}$	$\bar{s}^{+\sigma}$	$e^{\overline{\log(s)}}$
$l = 0$	WS	1.00^{+60}	30^{+360}	0.7
$l = 0, 2$	WS	$0.01^{+0.1}$	$0.09^{+0.18}$	0.02
$l = 0, 2, 4$	WS	$0.01^{+0.2}$	$0.14^{+0.70}$	0.02
$l = 0, 2, 4, 6$	WS	$0.01^{+0.1}$	$0.08^{+0.15}$	0.02
$l = 0$	CT	$0.4^{+0.6}$	$0.7^{+0.8}$	0.31
$l = 0, 2$	CT	$0.35^{+1.2}$	$1.1^{+3.8}$	0.27
$l = 0, 2, 4$	CT	$0.37^{+1.7}$	$1.4^{+7.1}$	0.27
$l = 0, 2, 4, 6$	CT	$0.30^{+0.7}$	$0.8^{+1.6}$	0.27

This perspective is reinforced by binning the data in 25%, 50%, and 75% ellipticity s quartiles. In Table VII we notice that the parametrizations that use a softened density profile provide fits with a lower ellipticity than those that use a hard profile. The table shows that the third quartile is reached at 1 for the sharp density cutoff, and around 0.1 for the softer DM profile of Woods-Saxon: a majority of galaxies would qualify as having prolate DM haloes.

A few caveats certainly apply.

Many of the flat rotation curves (most galaxies in SPARC are of this type, see Sec. V D below) are never seen to turn downwards and start falling with r (even if they would at all: perfectly filamentary sources predict perfectly flat curves, although at the hundred kpc scale other galactic-scale bodies compete as sources of gravity). In those constant-V galaxies therefore, one cannot set a bound on the length of the major semiaxis a from any fitting procedure.

Using the database we can only wish to deduce the value of the semiaxis along the x- and y-axes, b, (if possible) and obtain an upper bound for the ellipticity, s, meaning that they might be even more prolate than our results suggest.

TABLE VII. Quartiles of the distribution for the ellipticity ratio $s = c/a$. It is clear that 75%, if not more, of the fit galaxies have a DM halo that is best described as prolate, with $s < 1$.

Multipole	Density	25%	50%	75%
$l = 0$	WS	0.99	0.99	1.00
$l = 0, 2$	WS	0.003	0.01	0.09
$l = 0, 2, 4$	WS	0.01	0.01	0.08
$l = 0, 2, 4, 6$	WS	0.01	0.01	0.09
$l = 0$	CT	0.12	0.40	1.00
$l = 0, 2$	CT	0.08	0.35	0.99
$l = 0, 2, 4$	CT	0.09	0.37	0.99
$l = 0, 2, 4, 6$	CT	0.09	0.30	0.99

During the fit of such flat rotation curve, the length of the semiaxis along the z-axis, a, will therefore hit the parameter boundary and stay there. This is visible in Fig. 26 where we see a large majority of fits requiring very large values for a, and many clustering at the low-end of s near zero.

In other galaxies, saliently dwarf ones (see Sec. V D below for a classification), $V(r)$ has positive derivative all the way to the end of the visible matter distribution and the fit can often not determine the halo shape either, as the full halo is not well probed.

In addition, the parametrizations with $l = 0, 2, 4$ seem to give more elongated halos than those with either $l = 0, 2$ or $l = 0, 2, 4, 6$, in concordance with Fig. 16.

C. Extraction of s from the multipole expansion of the DM density

In this subsection we obtain the ellipticity $s = c/a$ from the multipole expansion of the density in Sec. IV.

As shown in Fig. 27, which is analogous to Fig. 25, the behavior of the theoretical rotation curve depends on the ellipticity of the halo-density shape. In prolate haloes (violet line) $V(r) \sim$ constant when $b \leq r \leq a$ and in oblate haloes (orange line) $V(r)$ increases when $a \leq r \leq b$. When r finally clears the halo, the rotation curve must eventually decrease as the leading multipole's $V(r) \propto 1/\sqrt{r}$, which happens quickly when $r > a$ (for prolate haloes) or $r > b = c$ (for oblate ones). This expansion of the density is seen to yield, order by order, a more stable (less oscillatory) $V(r)$ curve than the one in which the potential is directly expanded (Fig. 25).

To explain rotation curves that become constant at large distances, the figure shows the need for elongated haloes. This translates into manifestly prolate haloes in the unexpanded model and higher order multipoles with a specific

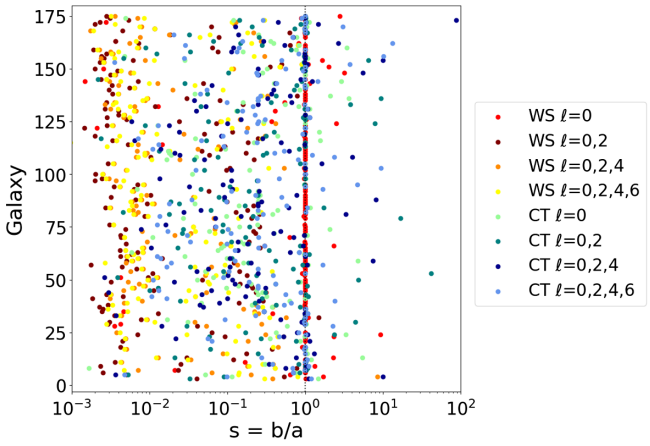

FIG. 26. Scatter plot of the ellipticity of fit DM haloes (x axis) for each galaxy (y axis) following the approach from Sec. III. Most of the fits fall in the $s \in (0, 1)$ region which describes haloes ranging from very prolate $s \sim 0$ to spherical $s = 1$.

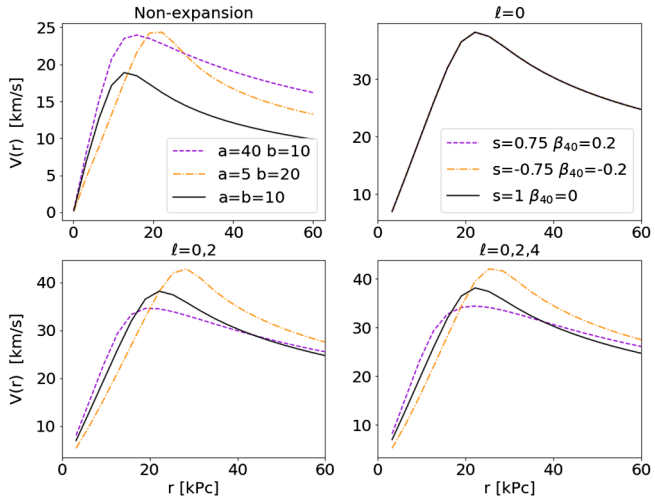

FIG. 27. Behavior of the rotation curve for the DM component upon expanding the DM density. The slowest falling dashed line (violet) is for an elongated halo, the fastest falling dashed-dotted (orange) corresponds to a flattened one and the black line is the reference spherical halo.

TABLE VIII. Parameters of the statistical distribution of s for the haloes in each parametrization of Sec. IV. From left to right, the columns display the angular parametrization, the density profile, the median and the average of $s = c/a$ with their one-sided uncertainties, and finally the geometric mean, that is well below 1 indicating the preference for prolateness.

Multipole	Density	MED$^{+\text{MAD}}$	$\bar{s}^{+\sigma}$	$e^{\overline{\log(s)}}$
Unexpanded	WS	$0.01^{+0.25}$	0.14^{+1}	<0.01
Unexpanded	CT	$0.05^{+0.8}$	0.5^{+3}	0.05
$l = 0$	WS	1	1	1
$l = 0, 2$	WS	$0.16^{+0.6}$	0.5^{+1}	0.22
$l = 0, 2, 4$	WS	$0.16^{+0.6}$	$0.5^{+1.2}$	0.24
$l = 0$	CT	1	1	1
$l = 0, 2$	CT	$0.16^{+0.9}$	$0.7^{+1.4}$	0.27
$l = 0, 2, 4$	CT	0.2^{+1}	$1^{+1.7}$	0.40

TABLE IX. Quartiles of the distribution of values obtained for the ellipticity ratio s. From left to right, the columns show the angular-dependence parametrization, the profile density and the maximum value of s reached within each quartile of the s distribution.

Angular shape	Density profile	25%	50%	75%
No-exp	WS	0.00	0.01	0.01
No-exp	CT	0.01	0.05	0.20
$l = 0$	WS	1.00	1.00	1.00
$l = 0, 2$	WS	0.16	0.16	0.16
$l = 0, 2, 4$	WS	0.16	0.16	0.16
$l = 0$	CT	1.00	1.00	1.00
$l = 0, 2$	CT	0.16	0.16	0.20
$l = 0, 2, 4$	CT	0.16	0.19	0.98

sign of β_{20} in the systematic expansion, whose leading behavior already appears with $l = 0, 2$ alone, $l = 4$ and higher bringing in incremental corrections.

In the "unexpanded" parametrization we again find that the ellipticity can be arbitrarily small, as explained in Sec. V B, due to those galaxies with ever-flattened rotation curves pulling the fit toward zero as much as we may allow it. This parametrization provides good fits, as seen in the earlier Table V, most of them leading to very elongated shapes (see Fig. 28). According to Tables VIII and IX, the shape of the haloes tends to be very elongated, similar to a thin cylinder. Most of the actual values seem to fall in the $s \in (0, 1]$ interval. The quartile distribution given in Table IX as well as the pictorial representation in Fig. 28 corroborate this.

Further, in Fig. 28 we see that this density-expansion parametrization assigns to the ellipticity values in the $s \in [0.16, 6.25]$ interval. In the case of $l = 0$, the ellipticity $s = 1$ is of course that of a spherical source. But in the case of a higher multipole contribution, the general trend is for the ellipticity to be for a very prolate object. Many of the fits hit the lowest interval bound $s = 0.16$ that we allow them to take.

The outcome of this analysis is that three quarters of the sampled galaxies prefer prolate dark matter haloes, and both median and geometric mean suggest typical ellipticities $s < 0.5$ and even of order 0.2 or less, whereas the arithmetic mean has too large an error to conclude anything: this is expected as it is not the appropriate variable for this analysis.

D. Correlating the galactic type and the ellipticity

The SPARC database contains information about the rotation curves for late type galaxies (that are expected to contain larger quantities of dark matter [61] and are thus ideal to probe it), of both spiral (S0, Sa, Sab, Sb, Sbc, Sc, Scd, Sd) and dwarf[4] types (Sdm, Sm, Im, BCD). The list of galaxies of each class is provided in Appendix V D.

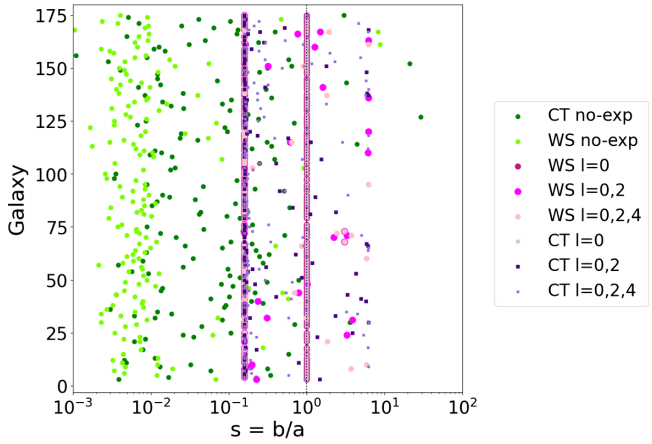

FIG. 28. Ellipticity of the fit haloes (x axis) for each galaxy (y axis) following the approach from Sec. IV. Most of the fits fall in the interval $s \in (0, 1]$, ranging from very prolate haloes $s \sim 0$ to spherical $s = 1$. The two salient vertical accumulation lines are at $s = 1$ (where the fits with $l = 0$ necessarily appear) and $s \simeq 0.16$ due to the lowest allowed s in some of the fits with constrained parameters.

We have discussed in earlier subsections of this Sec. V that we suspect many rotation curves to be incomplete due to a lack of data external to the galaxy. While in spiral galaxies the rotation curve flattens indefinitely (we do not observe a Keplerian fall-off in the rotation curve indicative that the entire halo would be contained within some radius R), in dwarf galaxies often we do not even reach that velocity plateau, and the rotation curve actually grows to the maximum r provided by the data. This entails that, generally speaking, dwarf galaxies seem to return worse fits than spiral galaxies (see Table X).

For both dwarf and spiral galaxies it is clear in the SPARC database that baryonic matter is insufficient to account for the rotations curves. The velocity profile in dwarf galaxies seems to be similar to that in spirals for small r, but to be chopped off earlier, before $V(r)$ flattens, probably due to the smaller size of dwarf galaxies even if they are believed to have a larger ratio of dark matter to visible matter. It is a reasonable hypothesis that currently the data is probing a smaller part of the halo for dwarfs than for spirals. Be it as it may be, dwarf galaxies have a variety of rotation-curve shapes.

From Fig. 29 we see that both the dwarf and spiral galaxy samples prefer a majority of prolate haloes, with sizeable counts of nearly spherical ones, but only a few fits yield

[4]In addition, dwarf galaxies are expected to be dominated by larger quantities of dark matter and are actively investigated in indirect γ-ray searches of dark matter [62].

TABLE X. Goodness of fit (median ± MAD of the $\chi^2/d.o.f.$ distribution for the galaxy sample) and the ellipticity (median) for 98 spiral galaxies and 51 dwarf galaxies taking into account all parametrizations of Secs. III and IV.

What is parametrized	Angular expansion	Density profile	Parametrization	Dwarf $\chi^2_D/d.o.f.$	Spiral $\chi^2_S/d.o.f.$	Ellipticity s_D	Ellipticity s_S
Density	Cylinder	Woods-Saxon	$R = R_0$	7.7 ± 4.9	3.0 ± 2.8	$\to 0$	$\to 0$
Density	Cylinder	Constant	$R = R_0$	8.0 ± 4.3	3.0 ± 4.1	$\to 0$	$\to 0$
Density	$l = 0$	Woods-Saxon	$R(\theta, s, \beta_{40}, R_0)$	9.0 ± 4.1	13.0 ± 3.1	1.00	1.00
	$l = 0, 2$	Woods-Saxon	$R(\theta, s, R_0)$	7.0 ± 3.0	11.0 ± 3.1	0.16	0.16
	$l = 0, 2, 4$	Woods-Saxon	$R(\theta, R_0)$	10.0 ± 3.1	11.0 ± 2.9	0.16	0.16
Density	$l = 0$	Constant	$R(\theta, s, \beta_{40}, R_0)$	17.0 ± 3.0	17.0 ± 1.6	1.0	1.0
	$l = 0, 2$	Constant	$R(\theta, s, R_0)$	16.0 ± 3.6	16.0 ± 4.0	0.16	0.16
	$l = 0, 2, 4$	Constant	$R(\theta, R_0)$	14.0 ± 3.4	14.0 ± 3.8	0.32	0.18
Potential	$l = 0$	Woods-Saxon	$R(\theta, a, b)$	11.0 ± 4.1	14.0 ± 2.9	0.99	0.99
	$l = 0, 2$	Woods-Saxon	$R(\theta, a, b)$	6.0 ± 2.9	9.0 ± 2.7	0.01	0.01
	$l = 0, 2, 4$	Woods-Saxon	$R(\theta, a, b)$	5.0 ± 3.2	7.0 ± 3.0	0.03	0.01
	$l = 0, 2, 4, 6$	Woods-Saxon	$R(\theta, a, b)$	5.0 ± 3.5	8.0 ± 3.1	0.05	0.01
Potential	$l = 0$	Constant	$R(\theta, a, b)$	11.0 ± 4.8	6.0 ± 4.0	0.96	0.31
	$l = 0, 2$	Constant	$R(\theta, a, b)$	11.0 ± 4.2	6.5 ± 4.4	0.95	0.25
	$l = 0, 2, 4$	Constant	$R(\theta, a, b)$	11.0 ± 4.8	5.0 ± 4.6	0.98	0.25
	$l = 0, 2, 4, 6$	Constant	$R(\theta, a, b)$	10.0 ± 4.7	7.0 ± 4.6	0.91	0.25
Density	No expansion	Constant	$R(\theta, a, b)$	12.0 ± 3.4	11.0 ± 3.9	0.04	0.05
	No expansion	Woods-Saxon	$R(\theta, a, b)$	7.0 ± 4.1	6.0 ± 3.3	0.01	0.01

oblate haloes in some parametrizations. Still, spirals seem to have a lower s ellipticity parameter in most of the models, indicating clearer prolateness of the halo.

As seen in Secs. III and IV, the proper value for the ellipticity cannot be determined, but an upper bound can be derived.

In most of our models, we see that for both, dwarfs and spirals, that halo ellipticity quotient $s = c/a$ (often an upper bound) falls in the interval $s \in (0, 1]$. In many spirals this is rather small, $s \in (0, 0.5]$, whereas dwarfs are better fit to have haloes with less elongated shapes, at least with present data.

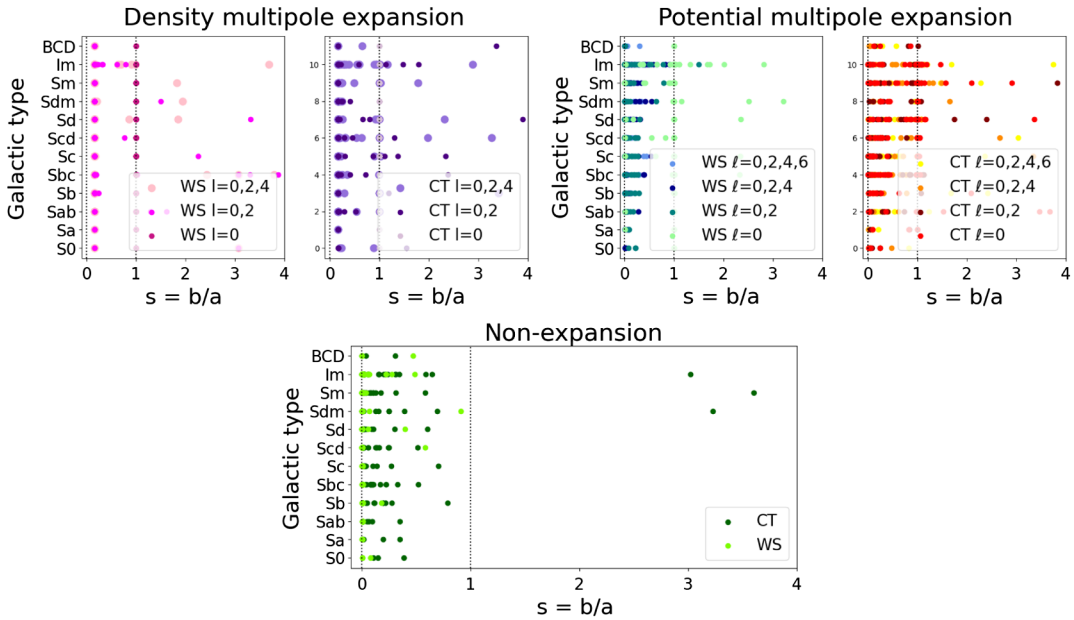

FIG. 29. Scatterplot of halo ellipticity fiting the SPARC database to the parametrizations in Secs. III and IV, breaking it by galactic category. The top four rows in each plot correspond to dwarf galaxies, and the rest are spirals. Galaxies to the right of the thin vertical line at $s = 1$ yield oblate haloes, those to the left, prolate ones.

VI. CONCLUDING DISCUSSION

We have reported fits to the galactic rotation curves obtained from SPARC's database [3] using several approaches. Because of the different number of parameters of each, a varying number of galaxies with few measured data points have been left out in each, in line with prior work [10]. In the analysis of Secs. III and IV we have left out the galaxies specified in Table XIII of the Appendix below, for the reasons explained there. In other analysis we have, however, included them, to avoid introducing too much overall bias.

From SPARC's own analysis [1] we have taken the basic data (distance to the galactic center r, total velocity $v \pm e$) but also the separate square velocity contributions for each component of visible matter. These comprise the bulge of the galaxy, its disk, and gas cloud. We have adopted their relation for the mass-to-light proportions $\Upsilon_{\rm bulge} = 1.4\Upsilon_{\rm disk}$ and $\Upsilon_{\rm disk} = 0.5 M_\odot/L_\odot$ [1,2] to be able to subtract the baryonic contribution to the rotation curve.

$$V_{{\rm B},i} = \sqrt{V^2_{i,{\rm gas}} + \Upsilon_{\rm bulge} V^2_{i,{\rm bulge}} + \Upsilon_{\rm disk} V^2_{i,{\rm disk}}} \quad (59)$$

(with i labeling each galaxy) and our actual fits refer to the rest, $V_{\rm DM}$, presumably due to the dark matter distribution, with the total velocity as in

$$V = \sqrt{V^2_{\rm DM} + V^2_B}. \quad (60)$$

Different approaches were contrasted against an adequately defined χ^2 function [53,63],

$$\chi^2 = \sum_{i=1}^{N} \frac{(V_{\rm th} - V_{\rm obs})^2}{e^2_{\rm obs}}. \quad (61)$$

We normalized this per degree of freedom, $\chi^2/(N-k)$ by dividing through the difference between the number N of data points for each galaxy and the number of fit parameters k.

Farrar and Loizeau also performed analogous fits to the rotation curves in [10]; further models can be seen there. Their generic conclusion is that the Einasto profile, or also even an additional disk component, would provide a better fit than traditional dark matter models or self-interacting dark matter.

A main feature of our allowing the use of elongated shapes is that the flatness of the rotation curves is more natural, leaving much more freedom to the underlying dark matter profiles as function of the distance, that do not need to be perfectly isothermal and therefore the underlying microscopic physics [64] is less constrained. Overall, we do find that fits with prolate haloes are preferred for nonfine-tuned radial dark matter density profiles (in those that approach the precise $\rho \sim 1/r^2$ power-law form there is quite some degeneracy in describing $V(r)$ for large r and the shape cannot reliably be extracted).

A. Comparison with large-scale numerical simulations and other work

In the simulations reported by Allgood *et al.* and other works [65–68], the dark matter halo distribution was found to be slightly triaxial, and somewhat more prolate than oblate, with a mean ellipticity compatible with our typical values. However, those authors do not seem to stress the point that a few of the galaxies that are very oblate are actually pulling the fit toward oblateness, when a significant majority of them is actually prolate, some being extremely prolate, and this providing what should become a textbook explanation for the flatness of rotation curves.

In fact, the procedure of quoting an arithmetic average of the ellipticity a/c is obscuring the actual stand of the galaxy population. A quick way to see it is that the average of two numbers, 0.33333 and 3, the first of which is as prolate as the second is oblate, becomes $1.666 > 1$ which is clearly oblate. However this population of two galaxies should be neutral and yield an average spherical shape, with $\langle s \rangle = \langle a/c \rangle = 1$. Obviously, the correct averaging procedure for a variable distributed over $(0, \infty)$ with neutral point at $s = 1$ is to work in a logarithmic scale.

Therefore we propose to average the natural logarithm $\langle \log(s) \rangle$ (this is equivalent to using the geometric mean instead of the arithmetic mean of the distribution of s) over

TABLE XI. Average ellipticities of dark matter haloes extracted by various methods; and approximate average values in the logarithmic scale that we advocate. If known for several halo masses, we quote s for the large haloes that can host typical spiral galaxies.

Method	s	$\log s$	References
Weak lensing	0.66(0.07)	−0.41(0.11)	[69]
Fit galactic $V(r)$		−3.6(4.7)	This work (Sec. V A, uncleaned sample)
Fit galactic $V(r)$	$0.14^{+0.7}$	−1.4	This work (Sec. V B, curated sample)
Fit galactic $V(r)$	$0.5^{+1.2}$	−4	This work (Sec. V C, curated sample)
Simulations at $z = 0$	$\simeq 0.6$		[65]

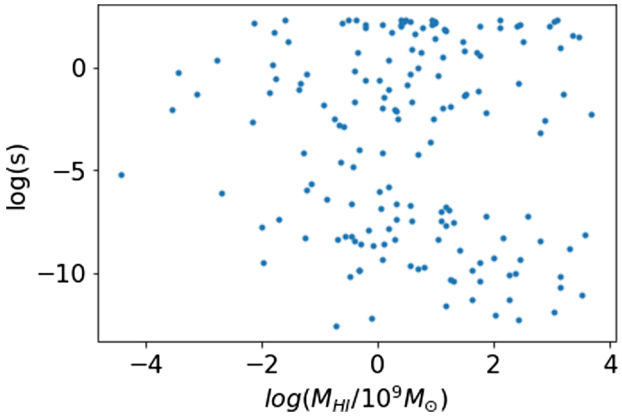

FIG. 30. We fail to find a visible correlation between the presumed dark-matter halo ellipticity and the visible galactic mass (that, by the Tully-Fisher relation, is normally taken proportional to the total mass).

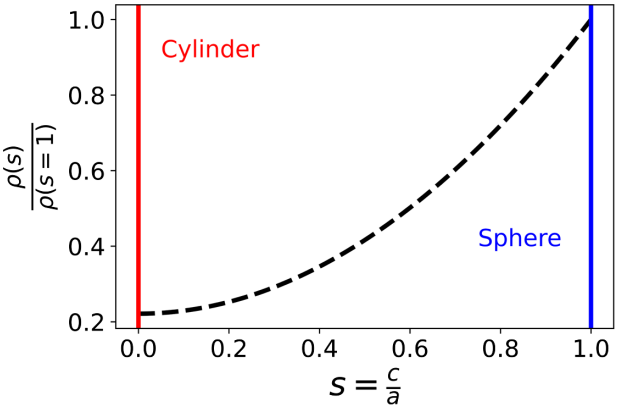

FIG. 31. A prolate halo implies less dark matter in the galactic plane: we show the ratio to a spherical shape, other things being equal. This would mean that extractions of DM-nucleon cross-sections in the laboratory are affected by a further factor larger than 2.

the galaxy sample, and have obtained, for example in Sec. V A,

$$e^{\langle \log(s) \rangle} = 0.026 \tag{62}$$

which is distinctly smaller than unity. This indicates a rather prolate distribution of galaxies, though with a broad shoulder of some oblate ones as indicated by a spread [0.0002, 2.783].

A second, independently coded analysis based on a spherical-harmonic expansion, yields a median $s \simeq 0.01^{+0.20}$ for the $l = 0, 2, 4$ parametrization in Sec. III and $s \simeq 0.16^{+0.60}$ for the $l = 0, 2, 4$ parametrization in Sec. IV. Various other parametrizations seem to be broadly consistent with these.

Table XI presents arithmetic and geometric averages of these and other shape analysis, including one based on weak lensing that we have located in the literature [69]. Apparently the lensing data is also suggestive of an average prolate halo, and once more the authors seem to be using an arithmetic average over s.

We quote, for the cosmological simulation entry, a number of 0.6 that broadly describes what is reported in Fig. 1 of that Ref. [65], at $z = 0$. Those authors have also extracted the dependence with the cosmological redshift z and with the galaxy mass $M_{\rm galaxy}$. They see a clear correlation $s(M)$ that we cannot confirm at this point, as shown in Fig. 30. However we have found a correlation with the galaxy shape, with spiral ones having smaller s and elliptical ones larger s (Sec. V D)

B. Final comments

Additionally to gravitational lensing and the rotation curves, further confirmation of the shape of the halo may come from studying observables outside the galactic plane, such as stellar streams [70]. Broadly, in the presence of such halo the movement perpendicular to the galactic rotation axis, not too far from the galactic plane, is the same as for a spherical distribution with changed parameters, and the vertical motion is that of an oscillator, with the orbital plane precessing [12].

These results are of impact to the direct laboratory detection programme. As shown in Fig. 31, as the deformation of the halo toward prolateness increases, less dark matter is to be found in the galactic disk. This entails that estimates of dark matter therein are overestimated, typically by a factor 2, which is affecting the extracted bounds on dark matter-nucleon cross-sections.

We think we have exhaustively employed the information at hand, but there is room for future improvements. For example, one roadblock that we have found is that some galaxies have rotation curves that are flat right out of $r = 0$, for example NGC5371 or NGC5907; in this cases, the usual low-r growth of $V(r)$ is not visible. This introduces model distortions that affect our fits; basically only an infinitely thin filament could fit that rotation curve. This probably happens because the identification of the point $r = 0$ in the galactic plane has not been fully achieved by the observational collaboration (since galaxies are most often seen at oblique angles). To reduce this uncertainty in our fits, we would need "better" data, which is of course beyond our ability as it depends on the observational program.

ACKNOWLEDGMENTS

We thank our engineer David Fernández Sanz for maintaining an adequate computing environment suited to our needs at the theoretical physics departmental cluster, and C. Pieterse and N. Loizeau for useful conversations. Financially supported by spanish Grant No. MICINN: PID2019–108655 GB-I00 (Spain), and Universidad Complutense de Madrid under research group 910309 and the IPARCOS, Institute for Particle and Cosmos physics institute.

TABLE XII. List of galaxies that do not favor a prolate dark matter halo shape, assigned to specific behavior classes as described in the text.

Class	Galaxies
1 (Oscillating)	UGC02916 NGC2903 NGC2955 NGC3877 NGC4051 NGC4138
2 (Uncertain)	F561-1 UGC04305
3 ($V_{\rm DM}(r)$ ever growing)	F568-3 F571-8 IC4202 NGC0055 NGC2903 NGC3769 NGC4157 NGC4217 NGC4389 NGC5005 NGC5055 NGC6195 NGC7331 UGC02455 UGC06614 UGC06973 UGC07866 UGC09037
4 (small r)	NGC3893 UGC05986
5 ($V_{\rm DM}(r) \simeq 0$ at large radii)	PGC51017 UGC06628

The authors have no conflict of interest.

O. M. C. is responsible for the codes and reporting of Secs. II and V A. A. B. Q. wrote an independent program and reported the results of Secs. III, IV, V B, V C, and V D. F. J. L.-E. designed and directed the investigation, and is responsible for the manuscript's draft.

APPENDIX: CLASSIFICATION OF GALAXIES WITHOUT STRAIGHTFORWARD ROTATION CURVES

1. Galaxies with fits typically yielding oblate haloes

In this appendix we first provide a classification of, and list, the galaxies that are seemingly actually best fit by an oblate shape than a prolate shape depending on the analysis, as they form a distinct minority of the SPARC database that reduces the force of the main result of the article, so they need individual understanding.

We have found that the dark matter velocity component $V_{\rm DM}$ in Eq. (13) of some of these galaxies keeps growing at large r. That means that the edge of their dark matter distribution has not been reached and thus we cannot really find out the shape of the DM halo. These galaxies are assigned to class 3 in Table XII.

A few other galaxies have properties that make the fitting with a prolate halo difficult, and are also listed in Table XII.

Those in class 1 are affected by large oscillations in the $V_{\rm DM}$ pseudodata at short distances r (see Fig. 24). This happens because the estimated contribution from the visible matter to the rotation curve is larger than the rotation curve itself at some points; therefore we cannot really trust the extraction of the pseudodata that has to be assigned to dark matter.

The two galaxies in class 2 have very large data uncertainty, so while they come out oblate they are not very significant.

In turn, the data for the two galaxies in class 4 reaches small distance only, $r < 4a$ respect to the ellipsoid axis, where the dependence of the rotation curve on s is smaller (see Fig. 21).

Finally, there are two galaxies that we assign to a class 5 that have quite an anomalous behavior unlike other spirals, with a rotation curve that starts off at 20 kpc and after a quick decrease to $V_{\rm DM} \sim 0$ stay there for large distances (ironically, this behavior is closer to what Kepler's law would make us expect, though the slope is too steep).

At least one of the galaxies analyzed, NGC2903, simultaneously belongs to two categories, in this case 1 and 3, because in addition to a never-decreasing rotation curve, it presents significant oscillations.

Having achieved some understanding of why a fraction of the galaxy sample favors an oblate halo shape, we feel confident that a good explanation for the flattening of $V(r)$

TABLE XIII. List of galaxies that are rejected in Secs. III and IV, possibly due to deficiencies in the extraction of the part of the rotation curve $V_{\rm DM}(r)$ assignable to dark matter. They are broken into two specific behavior classes, one corresponding to the baryonic matter alone overpredicting the rotation curve, let alone any dark matter (this seems to be sufficient reason to doubt the observational measurements and put them on hold) and the second due to insufficient data near $r = 0$ to have a fittable shape by something other than an infinite filament or similar.

Class	Galaxies
1 ($V(r)_{\rm baryons} > V_{\rm exp}(r)$ near $r = 0$ measurement error?)	CamB, NGC4217, NGC4389, UGC02455,
2 (Not enough data around center of galaxy)	D512-2, F565-V2, F567-2, F568-1, F574-1, F574-2, F579-V1, NGC6789, PGC51017, UGC00191, UGC00634, UGC00891, UGC02023, UGC05829, UGC05999, UGC07232, UGC08699, UGC09992,

for the typical spiral galaxy, the majority behavior, can be the prolateness of the dark matter distribution.

2. Galaxies rejected in Secs. III and IV on the grounds of strongly distorted rotation curves and similar

In Secs. III and IV we have rejected some of the galaxies from SPARC's database and not included them in the fits there due to questions about the data. The classification of those problems with $V(r)$ is provided in Table XIII. In this case we have left out two types of galaxies as seen in the table: one due to the fact that the experimental baryonic rotation curve falls above the total rotation curve of the galaxy, and the other due to the scarcity of data near $r = 0$.

[1] F. Lelli, Stacy S. McGaugh, and James M. Schombert, Astron. J. **152**, 157 (2016).
[2] F. Lelli, Dissertation, University of Groningen, 2013, https://research.rug.nl/files/14424281/thesis-lelli.pdf.
[3] SPARC Database, http://astroweb.cwru.edu/SPARC/.
[4] H. W. Babcock, Lick Obs. Bull. **498**, 41 (1939).
[5] H. C. van de Hulst *et al.*, Rev. Mod. Phys. **30**, 913 (1958).
[6] L. M. J. S. Volders, Bull. Astron. Inst. Neth. **14**, 323 (1959), https://articles.adsabs.harvard.edu/pdf/1959BAN....14..323V.
[7] G. Bertone and D. Hooper, Rev. Mod. Phys. **90**, 045002 (2018).
[8] V. C. Rubin *et al.*, Astrophys. J. Lett. **225**, L107 (1978).
[9] N. Bar, K. Blum, and C. Sun, Phys. Rev. D **105**, 8 (2022).
[10] N. Loizeau and G. R. Farrar, Astrophys. J. Lett. **920**, L10 (2021).
[11] C. Mihos *et al.*, Astrophys. J. **762**, 82 (2012).
[12] F. J. Llanes-Estrada, Universe **7**, 346 (2021); This is an independent rediscovery of a basic observation that a handful of scientists have made but that has not permeated the mainstream, see e.g., B. A. Slovick, arXiv:1009.1113.
[13] J. S. Jaracz, arXiv:2302.09720.
[14] G. U. Varieschi, Mon. Not. R. Astron. Soc. **503**, 1915 (2021); G. Calcagni and G. U. Varieschi, J. High Energy Phys. 08 (2022) 024.
[15] A. Giusti, Phys. Rev. D **101**, 124029 (2020).
[16] K. Zatrimaylov, J. Cosmol. Astropart. Phys. 04 (2021) 056.
[17] C. Rodrigo-Blanco and J. Perez-Mercader, Astron. Astrophys. **330**, 474 (1998), https://adsabs.harvard.edu/full/1998A%26A...330..474R; Carlos Rodrigo Blanco, Dissertation, Universidad Complutense de Madrid, 1999.
[18] M. Khelashvili, A. Rudakovskyi, and S. Hossenfelder, arXiv:2207.14165.
[19] A. B. Quintana, F. J. Llanes-Estrada, and O. M. Carretero, Proc. Sci. EPS-HEP2021 (**2021**) 137 [arXiv:2109.11153].
[20] J. F. Navarro, C. S. Frenk, and S. D. M. White, Mon. Not. R. Astron. Soc. **275**, 720 (1995).
[21] L. Hernquist, Astrophys. J. **356**, 359 (1990).
[22] S. S. McGaugh and J. M. Schombert, Astron. J. **148**, 77 (2014).
[23] R. B. Tully and J. R. Fisher, Astron. Astrophys. **54**, 661 (1977), https://articles.adsabs.harvard.edu/full/1977A%26A....54..661T.
[24] R. Sancisi, IAU Symp. **220**, 233 (2004).
[25] M. Milgrom, Astrophys. J. **270**, 365 (1983).
[26] M. Milgrom, Astrophys. J. **270**, 371 (1983).
[27] M. Milgrom, Astrophys. J. **270**, 384 (1983).
[28] B. Famaey and J. Binney, Mon. Not. R. Astron. Soc. **363**, 603 (2005).
[29] S. Dodelson and M. Liguori, Phys. Rev. Lett. **97**, 231301 (2006).
[30] A. Aguirre, J. Schaye, and E. Quataert, Astrophys. J. **561**, 550 (2001).
[31] D. Clowe, A. Gonzalez, and M. Markevitch, Astrophys. J. **604**, 596 (2004).
[32] R. G. Vishwakarma, Int. J. Mod. Phys. D **30**, 2142006 (2021).
[33] J. Brandbyge and S. Hannestad, J. Cosmol. Astropart. Phys. 10 (2017) 015.
[34] P. Mocz *et al.*, Phys. Rev. Lett. **123**, 141301 (2019).
[35] W. J. G. de Block, Adv. Astron. **2010**, 1 (2010).
[36] A. Del Popolo and F. Pace, Astrophys. Space Sci. **361**, 162 (2016).
[37] T. M. C. Abbott *et al.*, Astrophys. J. **872**, L30 (2019).
[38] C. Carignan, L. Chemin, W. K. Huchtmeier, and F. J. Lockman, Astrophys. J. Lett. **641**, L109 (2006).
[39] J. Cooley, Phys. Dark Universe **4**, 92 (2014).
[40] H. J. de Vega, P. Salucci, and N. G. Sanchez, New Astron. **17**, 653 (2012).
[41] S. Mitra, Phys. Rev. D **70**, 103517 (2004).
[42] G. D. Mack, J. F. Beacom, and G. Bertone, Phys. Rev. D **76**, 043523 (2007).
[43] S. Weinberg, *Cosmology* (Oxford University Press, Oxford, 2008), ISBN 978-0-19-852682-7.
[44] J. N. Bahcall and R. M. Spheira, Astrophys. J. Suppl. Ser. **44**, 73 (1980).
[45] J. Einasto and U. Haud, Astron. Astrophys. **223**, 89 (1989), https://adsabs.harvard.edu/full/1989A%26A...223...89E.
[46] J. L. Sersic, Bol. Asoc. Argent. Astron. La Plata Argent. **6**, 41 (1963), http://sedici.unlp.edu.ar/bitstream/handle/10915/73765/Bolet%C3%ADn_Completo.pdf?sequence=1&isAllowed=y.
[47] G. de Vaucouleurs, Mon. Not. R. Astron. Soc. **113**, 134 (1953).
[48] D. H. Jones *et al.*, Mon. Not. R. Astron. Soc. **399**, 683 (2009).
[49] S. Alam *et al.*, Astrophys. J. Suppl. Ser. **219**, 12 (2015).
[50] V. Springel *et al.*, Nature (London) **435**, 629 (2005).
[51] R. D. Woods and D. S. Saxon, Phys. Rev. **95**, 577 (1954).
[52] J. Binney and S. Tremaine, *Galactic Dynamics* (Princeton University Press, Princeton, NJ, 1987).
[53] The description of `iminuit` for Python is credited to H. Dembinski *et al.*, 10.5281/zenodo.5068904(2021).

[54] M. G. Kendall and B. B. Smith, Ann. Math. Stat. **10**, 275 (1939).
[55] J. L. Hodges, Jr and E. L. Lehmann, Ann. Math. Stat. **27**, 324 (1956).
[56] See Supplemental Material at http://link.aps.org/supplemental/10.1103/PhysRevD.107.083524 for data files with the fit χ^2 used in Sec. II C for public inspection, in plain text format.
[57] J. Binney and S. Tremaine, *Galactic Dynamics* (Princeton University Press, Princeton, NJ, 2008), 2nd ed.
[58] S-G. Zou, Phys. Scr. **91**, 063008 (2016).
[59] S. Frauendorf, Phys. Scr. **93**, 043003 (2018).
[60] J. Jia, Phys. Rev. C **105**, 014905 (2022).
[61] F. Combes, New Astron. Rev. **46**, 755 (2002).
[62] N. Torini, in *4th Workshop on Science with the New Generation of High Energy Gamma-Ray Experimental, MAGIC* (2007), pp. 61–68, 10.1142/9789812709653_0008.
[63] S. Sirca, *Probability for Physicists*, Graduate Texts in Physics (Springer, Cham, Switzerland, 2018); see also J. Gorgas and N. Cardiel, *Estadística básica para estudiantes de ciencias* (Universidad Complutense de Madrid, Madrid, 2009).
[64] P. H. Chavanis, Phys. Rev. D **106**, 043538 (2022).
[65] B. Allgood, R. A. Flores, J. R. Primack, A. V. Kravtsov, R. H. Wechsler, A. Faltenbacher, and J. S. Bullock, Mon. Not. R. Astron. Soc. **367**, 1781 (2006).
[66] M. Bonamigo, G. Despali, M. Limousin, R. Angulo, C. Giocoli, and G. Soucail, Mon. Not. R. Astron. Soc. **449**, 3171 (2015).
[67] J. Vega-ferrero, G. Yepes, and S. Gottlöber, Mon. Not. R. Astron. Soc. **467**, 3226 (2017).
[68] D. Ceverino, J. Primack, and A. Dekel, Mon. Not. R. Astron. Soc. **453**, 408 (2015).
[69] H. Hoekstra, H. K. C. Yee, and M. D. Gladders, IAU Symp. **220**, 439 (2004).
[70] A. Bonaca, M. Geha, A. H. W. Küpper, J. Diemand, K. V. Johnston, and D. W. Hogg, Astrophys. J. **795**, 94 (2014).